Memorandum 2008 (May 2013). ISSN 1874-4850. Available from: http://www.math.utwente.nl/publications
Department of Applied Mathematics, University of Twente, Enschede, The Netherlands

Variational space-time (dis)continuous Galerkin method for nonlinear free surface waves

E. Gagarina[a], J.J.W. van der Vegt[a], V.R. Ambati[a], O. Bokhove[a,b,*]

[a] *Mathematics of Computational Science Group*
Dept. of Applied Mathematics, University of Twente
P.O. Box 217, Enschede, The Netherlands.
[b] *School of Mathematics, University of Leeds*
LS2 9JT, Leeds, United Kingdom.

Abstract

A new variational finite element method is developed for nonlinear free surface gravity water waves. This method also handles waves generated by a wave maker. Its formulation stems from Miles' variational principle for water waves together with a space-time finite element discretization that is continuous in space and discontinuous in time. The key features of this formulation are: (i) a discrete variational approach that gives rise to conservation of discrete energy and phase space and preservation of variational structure; and (ii) a space-time approach that guarantees satisfaction of the geometric conservation law which is crucial in handling the deforming flow domain due to the wave maker and free surface motion.

The numerical discretization is a combination of a second order finite element discretization in space and a second order symplectic Stormer-Verlet discretization in time. The resulting numerical scheme is verified against nonlinear analytical solutions and discrete energy conservation is demonstrated for long time simulations. We also validated the scheme with experimental data of waves generated in a wave basin of the Maritime Research Institute Netherlands.

Keywords: nonlinear water waves, finite element method, Galerkin approximation, variational formulation, symplectic time integration, deforming grids

1. Introduction

The hydrodynamics of water waves in offshore regions of seas and oceans are of significant interest to naval architects and marine engineers. Particularly important is the dynamics of extreme wave phenomena, such as freak waves, and their effect on offshore structures and ships. Often engineers test prototype models of ships and offshore structures in experimental facilities, such as wave basins mimicking a realistic sea state. For extreme waves it is, however, nontrivial to generate waves with

*Corresponding author
Email addresses: E.Gagarina@utwente.nl (E. Gagarina), j.j.w.vandervegt@utwente.nl (J.J.W. van der Vegt), v.r.ambati@utwente.nl (V.R. Ambati), o.bokhove@leeds.ac.uk (O. Bokhove)

specific properties at the measurement locations in a wave basin. Numerical modeling of waves is therefore of tantamount importance to investigate the nature of waves generated by the wave maker and to locate extreme wave phenomena occurring in the wave basin.

A large class of water wave problems is described by the potential flow equation coupled with nonlinear free surface boundary conditions. These free surface gravity water wave equations are obtained from the Euler equations of fluid motion under the assumptions that the fluid is inviscid and incompressible and the velocity field irrotational (see Johnson [15]).

The free surface gravity water wave equations can also be obtained in a succinct way via Luke's variational principle [22] or from its dynamical equivalent presented by Miles [26]. The essence of the variational principle is that the complete problem can be expressed in a single functional. In addition, the variational formulation is associated with conservation of energy and phase space, under suitable boundary conditions. Approximate finite element solutions of the free surface water wave equations can be constructed either from a weak formulation or a variational formulation. Variational finite element formulations have as main benefit that they provide a natural setting to ensure discrete energy and phase space conservation leading to a stable numerical scheme.

Variational finite element formulations for free surface waves can be found in Kim and Bai [16] and Kim et al. [17]. Their formulation is, however, restricted to an unbounded domain and involves a coordinate transformation to a reference domain. Klopman et al. [18] derived a variational Boussinesq model from Luke's variational principle, which in essence is a vertical discretization of Luke's variational principle. Standard finite element methods for free surface gravity water waves can be found in [23, 24, 25, 39, 40, 41, 42]. Another widely used numerical method for free surface waves is the boundary integral method, which started with the work of Longuet-Higgins and Cokelet [21], and Vinje and Brevig [38]. This method has been applied extensively to two dimensional free surface waves, see the surveys of Romate [29] and Tsai and Yue [34]. Applications in three dimensions (3D) using boundary integral methods include [2, 3, 5, 6, 11, 14].

More recently, discontinuous Galerkin (DG) methods for elliptic problems, see the overview in Arnold et al. [1], have enabled researchers to model free surface water waves. In particular, space-time DG methods, in which time is considered as an additional coordinate and the problem is solved in $d+1$ space, with d the spatial dimension, are promising for free surface flows. Space(-time) DG finite element methods for free surface wave problems were developed in van der Vegt and Tomar [35], Tomar and van der Vegt [33], and van der Vegt and Xu [37].

The nonlinear free surface gravity water wave equations are difficult to solve and pose a number of numerical challenges:

(i) the solution of the governing equations depends on the position of the free surface, which is not known a priori;

(ii) the flow domain continuously deforms in time, not only due to the free surface motion, but also due to the presence of a wave maker, which requires the fulfillment of the geometric conservation law;

(iii) energy needs to be conserved in time for long-time simulations in order to minimize the numerical decay of the wave amplitude;

(iv) accurate dispersion properties are needed for complex wave interactions.

To cope with these challenges, we consider the development of a variational finite element method for nonlinear free surface gravity water waves based on the Miles variational principle together with a space-time approach.

The use of the space-time framework is motivated by the fact that it provides a very natural setting to satisfy the geometric conservation law on domains with time-dependent boundaries, e.g. due to the free surface or wave maker motion, as was demonstrated by Lesoinne and Farhat [20]. For the free surface water wave equations we consider a space-time finite element discretization using a polynomial approximation that is continuous in space and discontinuous in time. A discrete variational formulation of the nonlinear water wave equations is obtained by substituting the polynomial expansions of the variables into the Lagrangian functional defined by Miles' variational principle. Applying now the variational principle to the discrete Lagrangian functional a system of (non)linear algebraic equations for the free surface and velocity potential is obtained. It is crucial that in the variational procedure the mesh deformation due to the free surface and wave maker motion is taken into account since the nodal coordinates depend on the wave height and wave maker position. This procedure will result in a stable numerical scheme that preserves a discrete energy and phase space.

Since the space-time domain is subdivided into a number of space-time slabs, with as boundaries the solution at times t^n and t^{n+1}, the Lagrangian functional is modified to account for the discontinuities in the flow field approximation across each space-time boundary and to establish a connection between two neighboring time intervals. For a linear approximation of the flow field in time, the space-time variational finite element discretization results in a time discretization that is similar to the symplectic Stormer-Verlet time discretization. The symplectic Stormer-Verlet time discretization is well suited for the variational finite element discretization of the nonlinear water wave equations when a wave maker is absent. In the presence of a wave maker, the symplectic Stormer-Verlet time discretization gives rise to an ambiguity about the time level where the wave maker position should be computed. The proper choice of the wave maker position is obtained from the requirement that the geometric conservation law must be satisfied. This is guaranteed if the wave maker position is taken half way between two time levels.

The variational finite element discretization resulting from the Miles variational principle for nonlinear free surface water waves results in a system of nonlinear algebraic equations. The first two steps in the time integration are implicit, and the third step is explicit, which is similar to the Stormer-Verlet time discretization described in Hairer et al. [13]. The nonlinear equations during the implicit steps are solved using an Newton method.

The matrix for the Newton method is very sparse. The sparsity depends directly on the number of nodes surrounding each global node in the flow domain. The need to use sparse matrix storage routines and sparse iterative or direct solvers led us to the PETSc package (see [30, 31, 32]) for assembling and solving the linear systems resulting from the Newton method for the solution of the variational finite element discretization.

The variational finite element method is first verified against a nonlinear exact solution constructed using Fenton's theory [7] for free surface waves in a periodic domain. The robustness and accuracy of the scheme is demonstrated by simulating these travelling waves for 100 time periods. It is also observed that the discrete energy fluctuates in time around a fixed value and the numerical wave amplitude does not decay even after a long time. A phase shift is, however, observed due to a numerical dispersion error, which can be reduced by choosing either a higher order time and/or space discretization.

The present numerical method is also validated against experimental data sets provided by the Maritime Research Institute Netherlands (MARIN). These experiments are conducted using two wave basin configurations, one with a varying bottom and the other one with a flat bottom. For both configurations, a piston type wave maker at one end of the domain and a beach at the other end of the domain are used. This experimental setup allows the generation of highly irregular waves and wave focussing, in which a slow moving wave train is overtaken by a fast moving wave train. More information on the experiments can be found in [12]. For all test cases, our numerical simulations agree well with the experimental data. Other numerical and theoretical methods applied to the same set-up are, e.g. [10] and [19].

The outline of this article is as follows. In Section 2, we present the Miles variational principle for nonlinear free surface waves and derive the governing equations. In Section 3, we present our new variational finite element formulation for nonlinear free surface waves. Subsequently, numerical verification against exact solutions and an extensive validation with experimental data are discussed in Section 4. Conclusions are drawn in Section 5.

2. Variational Description of Nonlinear Inviscid Water Waves

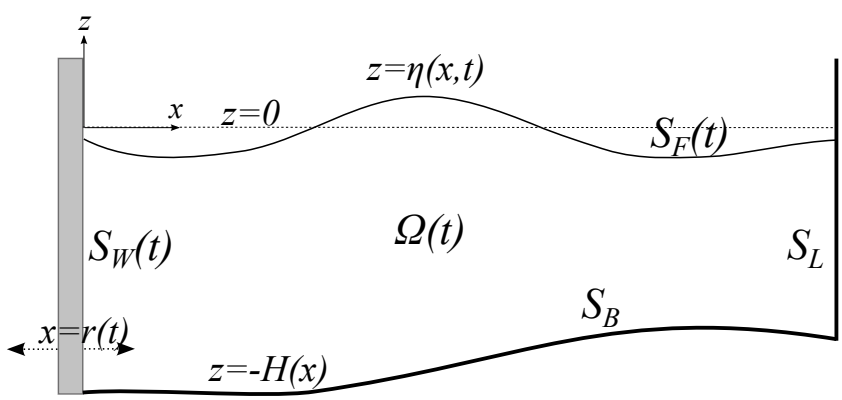

Figure 1: Sketch of wave basin with water waves generated by a piston type wave maker.

In this article we consider water waves generated by a wave maker in a wave basin. Assume that the fluid is inviscid, irrotational and incompressible. The dynamics of water waves evolving in the wave basin shown in Fig. 1 is then governed by the following functional (Miles [26]):

$$\mathcal{L}(\phi,\eta) := \int_0^T \left(\int_{r(t)}^L \phi_s \frac{\partial \eta}{\partial t} \mathrm{d}x - \int_{\Omega(t)} \frac{1}{2} |\nabla \phi|^2 d\Omega - \int_{r(t)}^L \frac{1}{2} g \eta^2 \mathrm{d}x - \int_{-H(0)}^{\eta} \frac{\mathrm{d}r}{\mathrm{d}t}\, \phi_w \, \mathrm{d}z \right) \mathrm{d}t, \qquad (1)$$

where (x, z) are the horizontal and vertical coordinates, respectively, ∇ the gradient operator, $\phi(x, z, t)$ the velocity potential, $\mathbf{u} := \nabla\phi$ the irrotational velocity field, and $\Omega \subset \mathbf{R}^2$ the time dependent flow domain. The boundaries of Ω are the free surface boundary S_F at $z = \eta(x, t)$, with η the free surface height, the bottom bed S_B at $z = -H(x)$, a piston type wave maker S_W at $x = r(t)$ and a solid wall S_L at $x = L$. Here, the wave maker is limited to horizontal movement only.

The variational principle for water waves is $\delta\mathcal{L} := \delta_\phi\mathcal{L} + \delta_\eta\mathcal{L} = 0$; where $\delta_\phi\mathcal{L}$ and $\delta_\eta\mathcal{L}$ are the variational derivatives with respect to ϕ and η, respectively. Evaluating the variational derivatives $\delta_\phi\mathcal{L}$ and $\delta_\eta\mathcal{L}$, we find

$$\delta_\phi\mathcal{L} := \int_0^T \left(\int_{r(t)}^L \frac{\partial\eta}{\partial t}\delta\phi_s \,\mathrm{d}x - \int_{\Omega(t)} \nabla\phi\cdot\nabla\delta\phi \,\mathrm{d}\Omega - \int_{-H(0)}^{\eta} \frac{\mathrm{d}r}{\mathrm{d}t}\,\delta\phi_w \,\mathrm{d}z \right)\mathrm{d}t, \tag{2a}$$

$$\delta_\eta\mathcal{L} := \int_0^T \left(\int_{r(t)}^L \phi_s \frac{\partial\delta\eta}{\partial t}\mathrm{d}x - \int_{r(t)}^L \frac{1}{2}|\nabla\phi|_s^2\delta\eta\mathrm{d}x - \int_{r(t)}^L g\eta\delta\eta\mathrm{d}x - \frac{\mathrm{d}r}{\mathrm{d}t}\,(\phi_s\delta\eta)_w \right)\mathrm{d}t, \tag{2b}$$

with the notation $(\cdot)_s = (\cdot)_{z=\eta}$ indicating the free surface and $(\cdot)_w = (\cdot)_{x=r(t)}$ the wave maker boundary. To take the variations with respect to the time-dependent boundary $z = \eta$ of the domain $\Omega(t)$ we used a variational analogue of the Reynolds transport theorem, as discussed in [9]. Integrating by parts (2a) in space and applying Gauss' divergence theorem; we obtain

$$\delta_\phi\mathcal{L} := \int_0^T \left(\int_{r(t)}^L \frac{\partial\eta}{\partial t}\delta\phi_s \,\mathrm{d}x + \int_{\Omega(t)} \nabla^2\phi\,\delta\phi \,\mathrm{d}\Omega - \int_{\partial\Omega(t)} (\mathbf{n}\cdot\nabla\phi)\delta\phi \,\mathrm{d}(\partial\Omega) - \int_{-H(0)}^{\eta} \frac{\mathrm{d}r}{\mathrm{d}t}\,\delta\phi_w \,\mathrm{d}z \right)\mathrm{d}t, \tag{3}$$

with $\partial\Omega := S_F \cup S_B \cup S_W \cup S_L$ and $\mathbf{n}$ the outward unit normal vector at the boundary $\partial\Omega$. Using the relations

$$\delta\phi_s = (\delta\phi)_s + (\partial\phi/\partial z)_s\delta\eta, \tag{4}$$

$$\int_{S_F} \mathrm{d}(\partial\Omega) = \int_{r(t)}^L |\nabla(z-\eta)|\mathrm{d}x, \tag{5}$$

$$\mathbf{n}|_{S_F} = \nabla(z-\eta)/|\nabla(z-\eta)|, \tag{6}$$

and after splitting the boundary integral into an integral over the different types of boundary faces, the variational derivative in (3) can be transformed into

$$\begin{aligned}\delta_\phi\mathcal{L} := \int_0^T \Bigg(&\int_{r(t)}^L \left(\frac{\partial\eta}{\partial t} - \nabla(z-\eta)\cdot\nabla\phi\right)_s (\delta\phi)_s \,\mathrm{d}x + \int_{r(t)}^L \frac{\partial\eta}{\partial t}\left(\frac{\partial\phi}{\partial z}\right)_s \delta\eta \,\mathrm{d}x + \int_{\Omega(t)} \nabla^2\phi\,\delta\phi \,\mathrm{d}\Omega \\ &- \int_{S_L\cup S_B} (\mathbf{n}\cdot\nabla\phi)\delta\phi \,\mathrm{d}(\partial\Omega) + \int_{-H(0)}^{\eta} \left(\frac{\partial\phi}{\partial x} - \frac{\mathrm{d}r}{\mathrm{d}t}\right)_w (\delta\phi)_w \,\mathrm{d}z \Bigg)\mathrm{d}t.\end{aligned} \tag{7}$$

Integrating now (2b) by parts in time, applying Leibnitz' rule and the relation $\partial\phi_s/\partial t = (\partial\phi/\partial t)_s +$

$(\partial\phi/\partial z)_s(\partial\eta/\partial t)$; we obtain

$$\delta_\eta\mathcal{L} := \left[\int_{r(t)}^{L} \phi_s\delta\eta \mathrm{d}x\right]_{t=0}^{t=T} + \int_0^T \left(\frac{\mathrm{d}r}{\mathrm{d}t}\,(\phi_s\delta\eta)_w - \frac{\mathrm{d}r}{\mathrm{d}t}\,(\phi_s\delta\eta)_w\right)\mathrm{d}t$$
$$- \int_0^T \left(\int_{r(t)}^{L} \left(\frac{\partial\phi}{\partial t} + \frac{1}{2}|\nabla\phi|^2 + g\eta\right)_s \delta\eta \mathrm{d}x + \int_{r(t)}^{L} \frac{\partial\eta}{\partial t}\left(\frac{\partial\phi}{\partial z}\right)_s \delta\eta \mathrm{d}x\right)\mathrm{d}t. \tag{8}$$

The nonlinear free surface gravity water wave equations now arise from the variational principle $\delta\mathcal{L} := \delta_\phi\mathcal{L} + \delta_\eta\mathcal{L} = 0$ by substituting the variational derivatives (7) and (8), imposing the end point conditions $(\delta\eta)_{t=0} = (\delta\eta)_{t=T} = 0$, and using the arbitrariness of the variations

$$\begin{aligned} \nabla^2\phi = 0 \quad &\text{on} \quad \Omega(t), \\ \partial_t\eta - \nabla(z-\eta)\cdot\nabla\phi = 0 \quad &\text{and} \quad \partial_t\phi + \frac{1}{2}|\nabla\phi|^2 + g\eta = 0 \text{ on } S_F(t), \\ \frac{\partial\phi}{\partial x} = \frac{\mathrm{d}r}{\mathrm{d}t} \text{ on } S_W(t), \quad &\text{and} \quad \mathbf{n}\cdot\nabla\phi = 0 \text{ on } S_B \cup S_L. \end{aligned} \tag{9}$$

As initial conditions we take the flow at rest, viz. $\phi(x,z,0) = 0$ in Ω and $\eta(x,0) = 0$ at S_F, and the waves are generated by the wave maker using a prescribed motion $x|_{S_W} = r(t)$.

3. Variational Finite Element Formulation

3.1. Space-time formulation

The computation of free surface gravity water waves is complicated due to the fact that the flow domain Ω changes with time and the fact that free surface S_F is part of the solution of the water wave equations. This requires a time-dependent mesh in order to follow the motion of the free surface and the wave maker. A very natural way to describe these problems is the space-time framework in which time is considered as an additional coordinate and the problem is solved in $d+1$ dimensional space, with d the spatial dimension of the domain, see e.g. [36, 37].

In the space-time formulation of free surface gravity water waves we consider the problem directly in the space-time domain $\mathcal{E} \subset \mathbb{R}^3$. A point $\mathbf{x} \in \mathbb{R}^3$ has coordinates $\mathbf{x} = (t,x,z) =: (t,\bar{\mathbf{x}})$. The flow domain $\Omega(t)$ at time t is defined as $\Omega(t) := \{\bar{\mathbf{x}} \in \mathbb{R}^2 \,|\, (t,\bar{\mathbf{x}}) \in \mathcal{E}\}$. The space-time domain boundary $\partial\mathcal{E}$ consists of the hypersurfaces $\Omega(t^0) := \{\mathbf{x} \in \partial\mathcal{E} \,|\, t = t^0\}$, $\Omega(T) := \{\mathbf{x} \in \partial\mathcal{E} \,|\, t = T\}$ and $\mathcal{Q} := \{\mathbf{x} \in \partial\mathcal{E} \,|\, 0 < t < T\}$. The space-time boundary $\mathcal{Q}$ is subdivided as $\mathcal{Q} := \mathcal{S}_F \cup \mathcal{S}_W \cup \mathcal{S}_B \cup \mathcal{S}_L$, with $\mathcal{S}_F$ and $\mathcal{S}_W$ describing, respectively, the evolution of the free surface and the wave maker in space-time, with $S_F(t) = \mathcal{S}_F \cap \{t\}$, $S_W(t) = \mathcal{S}_W \cap \{t\}$. The flow domain bottom in space-time is denoted $\mathcal{S}_B = S_B \times (t^0, T)$ and the end wall as $\mathcal{S}_L = S_L \times (t^0, T)$.

Using the partition $t^0 < \cdots < t^n < \cdots < t^N = T$ of the time interval (t^0, T) we can subdivide the space-time domain $\mathcal{E}$ into space-time slabs $\mathcal{E}^n := \{\mathbf{x} \in \mathcal{E} \,|\, t \in (t^n, t^{n+1})\}$ with $1 \le n \le N$. If the space-time boundary faces that are part of $\mathcal{Q}$ are restricted to the space-time slab $\mathcal{E}^n$ then we use the superscript n. The remaining boundaries of the space-time slab $\mathcal{E}^n$ are $\Omega^n = \Omega(t^n)$ and $\Omega^{n+1} = \Omega(t^{n+1})$.

The space-time slab $\mathcal{E}^n$ is tessellated with hexahedral space-time elements $\mathcal{T}_h^n$. The set of faces of the space-time elements at the free surface $\mathcal{S}_F^n$ and the wave maker $\mathcal{S}_W^n$ are denoted, respectively,

as Γ_F^n and Γ_W^n. The set of faces in Ω^n is denoted as Γ_{Ω^n}. Similarly, the set of faces at the free surface S_F^n and the wave maker S_W^n are denoted, respectively, as $\bar{\Gamma}_F^n$ and $\bar{\Gamma}_W^n$.

The tessellation $\mathcal{T}_h^n$ is constructed by first generating a mesh with quadrilateral elements in the domain $\Omega(t^n)$. The spatial elements are denoted as K_k^n, with k the element index in the tessellation. The set of quadrilateral elements K_n^k on Ω^n is denoted by $\bar{\mathcal{T}}_h^n$. Due to the free surface and wave maker motion the nodes of each element K_k^n will move to a new position at $t = t^{n+1}$, resulting in the spatial element K_k^{n+1}. The space-time elements $\mathcal{K}_k^n \in \mathcal{T}_h^n$ are then obtained by linear interpolation in time of the elements K_k^n and K_k^{n+1}. In general, the mesh deformation due to the domain boundary motion is unknown a priori and part of the solution. The geometry of the space-time elements is therefore continuously updated during the solution process.

In this article we will only consider structured meshes since the focus will be on the development of a novel variational finite element method. The mathematical formulation is, however, also applicable to unstructured meshes, but this extra geometrical flexibility is not necessary for the present study. The computational mesh in the space-time slab $\mathcal{E}^n$ contains N_x elements in the horizontal and N_z elements in the vertical direction. Nodes at the free surface and wave maker belong, respectively, to the sets $\mathcal{N}_F$ and $\mathcal{N}_W$, nodes in the interior of the domain Ω^n are collected in the set $\mathcal{N}_{\Omega^n}$ and nodes in $\overline{\Omega}^n \setminus S_F^n$, with $\overline{\Omega}^n$ the closure of Ω^n, in the set $\mathcal{N}_{\overline{\Omega}^n}$.

3.2. Function spaces and approximations

The construction of the basis functions in each space-time element is done in two steps. First, we define the mapping F_k^n between the spatial reference element $\widehat{K} = [-1, 1]^2$ and the finite element at time $t = t^n$, $K_k^n \subset \mathbb{R}^2$, as

$$F_k^n : \widehat{K} \to K_k^n : (\zeta_1, \zeta_2) \mapsto (x, z) := (x_{k,\alpha}^n, z_{k,\alpha}^n)\hat{\psi}_\alpha(\zeta_1, \zeta_2), \tag{10}$$

where $(x_{k,\alpha}^n, z_{k,\alpha}^n)$ are the coordinates of the vertices of element K_k^n at time t^n. The quadrilateral element K_k^n has element index k and its vertices are numbered as $\alpha = 1, ..., 4$. The functions $\hat{\psi}_\alpha(\zeta_1, \zeta_2)$ are the standard Lagrangian linear nodal basis functions and ζ_1, ζ_2 the coordinates of the reference element $\widehat{K}$. The summation convention is used on repeated indices. The basis functions $\varphi_{k,\alpha}^n$ on element K_k^n are then defined as

$$\varphi_{k,\alpha}^n(x, z) = \hat{\psi}_\alpha \circ (F_k^n)^{-1}(x, z).$$

The restriction of the basis functions $\varphi_{k,\alpha}^n$ to the face of K_k^n that is at the free surface S_F^n will be denoted as

$$\varphi_{s,k,\beta}^n(x) = \varphi_{k,\alpha}^n(x, \eta(x, t^n)),$$

with $\beta \in \{1, 2\}$ and $\alpha \in \{1, \cdots, 4\}$ the two vertices of element K_k^n that are at the free surface S_F^n.

The space-time basis functions are now defined directly in physical space using interpolation in time. We define basis functions that are linear in time in the space-time elements $\mathcal{K}_k^n \in \mathcal{T}_h^n$ and two sets of basis functions in space-time faces $\mathcal{S}_k^n$, which have different positions for the nodal variables.

These basis functions are defined as

$$
\begin{aligned}
P_1(\mathcal{K}_k^n) &:= \{\chi_{k,\alpha,1}^n, \chi_{k,\alpha,2}^n \,|\, \alpha = 1, \cdots, 4\},\\
Q_1(\mathcal{S}_k^n) &:= \{\chi_{s,k,\beta,1}^n, \chi_{s,k,\beta,2}^n \,|\, \beta = 1, 2\},\\
R_1(\mathcal{S}_k^n) &:= \{\chi_{s,k,\beta,3}^n, \chi_{s,k,\beta,4}^n \,|\, \beta = 1, 2\},
\end{aligned}
$$

with

$$
\begin{aligned}
\chi_{k,\alpha,1}^n &= \left(\frac{t^{n+1} - t}{\triangle t^n}\right) \varphi_{k,\alpha}^n, & \chi_{k,\alpha,2}^n &= \left(\frac{t - t^n}{\triangle t^n}\right) \varphi_{k,\alpha}^{n+1},\\
\chi_{s,k,\beta,1}^n &= \left(\frac{t^{n+1} - t}{\triangle t^n}\right) \varphi_{s,k,\beta}^n, & \chi_{s,k,\beta,2}^n &= \left(\frac{t - t^n}{\triangle t^n}\right) \varphi_{s,k,\beta}^{n+1},\\
\chi_{s,k,\beta,3}^n &= \left(\frac{t^n + t^{n+1} - 2t}{\triangle t^n}\right) \varphi_{s,k,\beta}^n, & \chi_{s,k,\beta,4}^n &= \left(\frac{2(t - t^n)}{\triangle t^n}\right) \varphi_{s,k,\beta}^{n+1/2},
\end{aligned}
$$

and $\varphi_{s,k,\beta}^{n+1/2} = \frac{1}{2}(\varphi_{s,k,\beta}^n + \varphi_{s,k,\beta}^{n+1})$. The time step $\triangle t^n = t^{n+1} - t^n$. The finite element approximation of the potential and wave height will use continuous basis functions in space and discontinuous basis functions in time. For this purpose the following finite element spaces are defined

$$
\begin{aligned}
V_h &:= \{v_h \mid v_h \in C^0(\mathcal{E}^n),\ v_h \in P_1(\mathcal{K}),\ \ \forall \mathcal{K} \in \mathcal{T}_h^n, n = 1, \cdots, N\},\\
W_h &:= \{v_h \mid v_h \in C^0(\mathcal{S}_F^n),\ v_h \in Q_1(\mathcal{S}),\ \ \forall \mathcal{S} \subset \mathcal{K} \cap \mathcal{S}_F^n,\ \mathcal{K} \in \mathcal{T}_h^n, n = 1, \cdots, N\},\\
Z_h &:= \{v_h \mid v_h \in C^0(\mathcal{S}_F^n),\ v_h \in R_1(\mathcal{S}),\ \ \forall \mathcal{S} \subset \mathcal{K} \cap \mathcal{S}_F^n,\ \mathcal{K} \in \mathcal{T}_h^n, n = 1, \cdots, N\}.
\end{aligned}
$$

The potential ϕ in the space-time slab $\mathcal{E}^n$ is now approximated as $\phi_h^t \in V_h$ and is represented in each space-time element $\mathcal{K}_k^n$ as

$$
\phi_h^t|_{\mathcal{K}_k^n} = \phi_k^n = \sum_{\alpha=1}^{4} \phi_{k,\alpha}^{n,+} \chi_{k,\alpha,1}^n + \phi_{k,\alpha}^{n+1,-} \chi_{k,\alpha,2}^n. \tag{11}
$$

In order to account for the discontinuity in time at the space-time slab boundary we use the superscript $+$ to indicate the nodal values for $t \downarrow t^n + 0^+$ and $-$ for $t \uparrow t_n - 0^+$, see Figure 2.

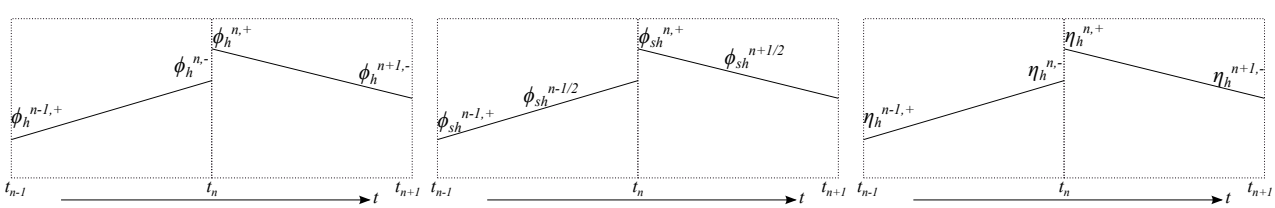

Figure 2: Piecewise linear approximation in time of coefficients $\eta_h, \phi_h, \phi_{sh}$.

The wave height η and potential at the free surface ϕ_s are now approximated in the space-time

free surface $\mathcal{S}_F$ as $\eta_h^t \in W_h$ and $\phi_{sh}^t \in Z_h$. In each space-time free surface face $\mathcal{S} \in \mathcal{S}_F^n$ the wave height and potential then can be expressed as

$$\eta_h^t|_{S_{F,k}^n} := \eta_k^n = \sum_{\beta=1}^{2} \eta_{k,\beta}^{n,+} \chi_{s,k,\beta,1}^n + \eta_{k,\beta}^{n+1,-} \chi_{s,k,\beta,2}^n, \tag{12}$$

$$\phi_{sh}^t|_{S_{F,k}^n} := \phi_{s,k}^n = \sum_{\beta=1}^{2} \phi_{s,k,\beta}^{n,+} \chi_{s,k,\beta,3}^n + \phi_{s,k,\beta}^{n+1/2} \chi_{s,k,\beta,4}^n, \tag{13}$$

with $\phi_{s,k,\beta}^{n+1/2} = \frac{1}{2}(\phi_{s,k,\beta}^{n,+} + \phi_{s,k,\beta}^{n+1,-})$. In order to simplify notation we also introduce the jump $[[.]]$ and average $\{\{.\}\}$ operators at each time level t^n, which are defined as

$$[[p^n]] = p^{n,-} - p^{n,+}, \quad \{\{p\}\}_{\gamma_1}^{\gamma_2} = \gamma_1 p^{n,-} + \gamma_2 p^{n,+}, \tag{14}$$

with $\gamma_1 + \gamma_2 = 1$ and $\gamma_1, \gamma_2 \geq 0$.

3.3. Discrete variational finite element discretization.

Substituting the space-time finite element approximations (11)-(13) to ϕ and η into the functional (1) we obtain the following discrete functional for the finite element approximation of Miles' variational principle

$$\begin{aligned}\mathcal{L}(\phi_h^t, \phi_{sh}^t, \eta_h^t, t) :&= \sum_{\mathcal{S}\in\Gamma_F^n} \int_{\mathcal{S}} \Big(\phi_{sh}^t \frac{\partial \eta_h^t}{\partial t} - \frac{1}{2} g (\eta_h^t)^2\Big) \mathrm{d}x\mathrm{d}t - \sum_{\mathcal{K}\in\mathcal{T}_h^n} \int_{\mathcal{K}} \frac{1}{2} |\nabla \phi_h^t|^2 \mathrm{d}x\mathrm{d}z\mathrm{d}t \\ &- \sum_{\mathcal{S}\in\Gamma_W^n} \int_{\mathcal{S}} \frac{\mathrm{d}r}{\mathrm{d}t} \phi_h^t \mathrm{d}z\mathrm{d}t - \sum_{\mathcal{S}\in\bar{\Gamma}_F^n} [[\eta_h^t]] \{\{\phi_{sh}^t\}\}_{\gamma_1}^{\gamma_2},\end{aligned} \tag{15}$$

with $\gamma_1 = 0, \gamma_2 = 1$. The last term in the discrete formulation of Miles' variational principle is a coupling term that is added to connect the free surface space-time faces $\mathcal{S}_F^n$ and $\mathcal{S}_F^{n-1}$. This contribution is necessary since the basis functions are discontinuous in time and the wave height and free surface potential would otherwise not be connected to the previous space-time slab. For more information, see [37]. In the space-time coupling term the jump in the wave height is weighted with the potential at $t^{n,+}$. This contribution can be derived using the theory of nonconservative products [4] for the time derivative in the discrete variational principle (15), see also [27], [28].

For the formulation of the algebraic system it is beneficial to define the following global matrices and vector

$$\begin{aligned} D_{kl}^n &:= -\sum_{S\in\bar{\Gamma}_F^n} \int_S \varphi_k \frac{\partial \varphi_l(x)}{\partial t} \mathrm{d}x, & M_{kl}^n &:= \sum_{S\in\bar{\Gamma}_F^n} \int_S \varphi_k \varphi_l \mathrm{d}x, \\ A_{kl}^n(\boldsymbol{\eta}) &:= \sum_{K\in\bar{\mathcal{T}}_h^n} \int_K (\nabla\varphi_k \cdot \nabla\varphi_l) \mathrm{d}x\mathrm{d}z, & W_k^n(\boldsymbol{\eta}) &:= \sum_{S\in\bar{\Gamma}_W^n} \int_S \frac{\mathrm{d}r}{\mathrm{d}t} \varphi_k \mathrm{d}z. \end{aligned} \tag{16}$$

The indices k, l refer to the global nodal indices in the mesh. In the variations of the discrete Miles functional it is important to note that the matrices A_{kl} and W_k implicitly depend on the nodal

values of the wave height $\boldsymbol{\eta}$ due to the coupling of the mesh with the free surface motion.

We now further evaluate the various contributions in the discrete variational formulation in (15). If we substitute the representations of η_h^t and ϕ_{sh}^t, given by (12)-(13), then we obtain for the first term

$$\begin{aligned}\sum_{\mathcal{S}\in\Gamma_F^n}\int_{\mathcal{S}}\phi_{sh}^t\frac{\partial\eta_h^t}{\partial t}\mathrm{d}x\mathrm{d}t &= \sum_{n=1}^{N}\sum_{S\in\bar{\Gamma}_F^n}\int_S\int_{t^n}^{t^{n+1}}\Big(\phi_l^{n+\frac{1}{2}}\varphi_l^{n+1/2}\frac{2(t-t^n)}{\triangle t^n}+\phi_l^{n,+}\varphi_l^n\frac{t^n+t^{n+1}-2t}{\triangle t^n}\Big)\\ &\qquad\Big(\frac{1}{\triangle t^n}\eta_k^{n+1,-}\varphi_k^{n+1}-\frac{1}{\triangle t^n}\eta_k^{n,+}\varphi_k^n\Big)\mathrm{d}t\mathrm{d}x\\ &= \sum_{n=1}^{N}\sum_{S\in\bar{\Gamma}_F^n}\int_S\phi_l^{n+\frac{1}{2}}\varphi_l^{n+1/2}(\eta_k^{n+1,-}\varphi_k^{n+1}-\eta_k^{n,+}\varphi_k^n)\mathrm{d}x. \qquad (17)\end{aligned}$$

The expression given in (17) is, however, not practical for a direct evaluation since it contains products of basis functions at different time levels. We will therefore transform this expression into a form where can directly relate it to the matrices defined in (16). For this purpose we add and subtract the terms $\eta_k^{n+1,-}\varphi_k^{n+1/2}$ and $\eta_k^{n,+}\varphi_k^{n+1/2}$ to the η-contribution in (17), resulting in

$$\begin{aligned}&\sum_{n=1}^{N}\sum_{S\in\bar{\Gamma}_F^n}\int_S\phi_l^{n+\frac{1}{2}}\varphi_l^{n+1/2}(\eta_k^{n+1,-}\varphi_k^{n+1}-\eta_k^{n,+}\varphi_k^n)\mathrm{d}x\\ &=\sum_{n=1}^{N}\sum_{S\in\bar{\Gamma}_F^n}\int_S\varphi_l^{n+1/2}\varphi_k^{n+1/2}\phi_l^{n+\frac{1}{2}}(\eta_k^{n+1,-}-\eta_k^{n,+})+\Delta t^n\phi_l^{n+\frac{1}{2}}\eta_k^{n+1,-}\left(\frac{\varphi_k^{n+1}-\varphi_k^{n+1/2}}{\Delta t^n}\right)\varphi_l^{n+1/2}\\ &\qquad+\Delta t^n\eta_k^{n,+}\phi_l^{n+\frac{1}{2}}\left(\frac{\varphi_k^{n+1/2}-\varphi_k^n}{\Delta t^n}\right)\varphi_l^{n+1/2}\mathrm{d}x.\end{aligned}$$

This expression can be further rearranged into

$$\begin{aligned}&\sum_{n=1}^{N}\sum_{S\in\bar{\Gamma}_F^n}\int_S\varphi_l^{n+1/2}\varphi_k^{n+1/2}\phi_l^{n+\frac{1}{2}}(\eta_k^{n+1,-}-\eta_k^{n,+})+\Delta t^n\phi_l^{n+\frac{1}{2}}\big(\eta_k^{n+1,-}+\eta_k^{n,+}\big)\frac{\varphi_k^{n+1}-\varphi_k^{n+1/2}}{\Delta t^n}\varphi_l^{n+1/2}\\ &\qquad+\Delta t^n\eta_k^{n,+}\phi_l^{n+\frac{1}{2}}\frac{\varphi_k^{n+1/2}-\varphi_k^n-\varphi_k^{n+1}+\varphi_k^{n+1/2}}{\Delta t^n}\varphi_l^{n+1/2}\mathrm{d}x\mathrm{d}z,\end{aligned}$$

where the last term is zero due to the definition of $\varphi^{n+1/2}=\frac{1}{2}(\varphi^n+\varphi^{n+1})$. Also, if we use the relation

$$\begin{aligned}\sum_{S\in\bar{\Gamma}_F^n}\int_S\frac{1}{\Delta t^n}\varphi_l^{n+1/2}(\varphi_k^{n+1}-\varphi_k^{n+1/2})\mathrm{d}x\mathrm{d}z &= \sum_{S\in\bar{\Gamma}_F^n}\int_S\frac{1}{2\Delta t^n}(\varphi_k^{n+1}-\varphi_k^n)\varphi_l^{n+1/2}\mathrm{d}x\mathrm{d}z\\ &= -\frac{1}{2}D_{kl}^{n+1/2}+O((\triangle t)^2),\end{aligned}$$

then we obtain an expression for (17) which can be expressed using the matrices defined in (16)

$$\sum_{\mathcal{S}\in\Gamma_F^n}\int_{\mathcal{S}}\phi_{sh}^t\frac{\partial\eta_h^t}{\partial t}\mathrm{d}x\mathrm{d}t=\sum_{n=1}^{N}M_{kl}^{n+1/2}\phi_l^{n+\frac{1}{2}}(\eta_k^{n+1,-}-\eta_k^{n,+})-\frac{1}{2}\Delta t^n\phi_l^{n+\frac{1}{2}}\big(\eta_k^{n+1,-}+\eta_k^{n,+}\big)D_{kl}^{n+1/2}. \quad (18)$$

Next, if we combine the second and third term in the discrete Miles functional (15) then we obtain the discrete approximation of the time integral of the Hamiltonian, which is the sum of the potential and kinetic energy

$$\sum_{n=1}^{N}\int_{t^0}^{T}\mathcal{H}_h^t(\phi_h^t,\phi_{sh}^t,\eta_h^t,t)dt:=\sum_{\mathcal{S}\in\Gamma_F^n}\int_{\mathcal{S}}\Big(\frac{1}{2}g(\eta_h^t)^2\Big)\mathrm{d}x\mathrm{d}t+\sum_{\mathcal{K}\in\mathcal{T}_h^n}\int_{\mathcal{K}}\frac{1}{2}|\nabla\phi_h^t|^2\mathrm{d}x\mathrm{d}z\mathrm{d}t. \quad (19)$$

The time integral of the Hamiltonian in each space-time slab is approximated using the following quadrature rule

$$\begin{aligned}\int_{t^n}^{t^{n+1}}\mathcal{H}_h^t(\eta_h^{\mathrm{t}},\phi_{sh}^t,\phi_h^t,t)\mathrm{d}t=\frac{\Delta t^n}{2}\Big(&\mathcal{H}_h^n(\eta_k^{n,+},\phi_l^{n+1/2},\phi_{i'}^{n,+},t^{n+1/2})\\&+\mathcal{H}_h^{n+1}(\eta_k^{n+1,-},\phi_l^{n+1/2},\phi_{i'}^{n+1,-},t^{n+1/2})\Big). \quad (20)\end{aligned}$$

The contributions $\mathcal{H}_h^n$ and $\mathcal{H}_h^{n+1}$ can be further evaluated as

$$\begin{aligned}\mathcal{H}_h^{n_p}(\eta_k^{n_p},\phi_l^{n+1/2},\phi_{i'}^{n_p},t^{n+1/2})=&\frac{1}{2}gM_{kl}^{n+1/2}\eta_k^{n_p}\eta_l^{n_p}+\frac{1}{2}A_{lj'}^{n+1/2}(\eta^{n_p})\phi_l^{n+1/2}\phi_{j'}^{n_p}+\frac{1}{2}A_{i'j'}^{n+1/2}(\eta^{n_p})\phi_{i'}^{n_p}\phi_{j'}^{n_p}\\&+\frac{1}{2}A_{lk}^{n+1/2}(\eta^{n_p})\phi_l^{n+1/2}\phi_k^{n+1/2}+\frac{1}{2}A_{i'k}^{n+1/2}(\eta^{n_p})\phi_{i'}^{n_p}\phi_k^{n+1/2}, \quad (21)\end{aligned}$$

with $n_p=n,+$ or $n+1,-$. Here the indices $i',j'\in\mathcal{N}_{\Omega^n}$, and $k,l\in\mathcal{N}_F$. Analogously, the time integral for the wave maker contribution can be approximated as

$$\begin{aligned}\sum_{\mathcal{S}\in\Gamma_W^n}\int_{\mathcal{S}}\frac{\mathrm{d}r}{\mathrm{d}t}\phi_h^t\mathrm{d}z\mathrm{d}t&=\sum_{n=1}^{N}\int_{t_n}^{t^{n+1}}W_m^t(\eta_h^t)\phi_h^t\mathrm{d}t\\&=\sum_{n=1}^{N}\frac{\Delta t^n}{2}\Big(W_q^{n+1/2}(\eta_q^{n,+})\phi_q^{n+1/2}+W_q^{n+1/2}(\eta_q^{n+1,-})\phi_q^{n+1/2}\\&\qquad+W_e^{n+1/2}(\eta_q^{n,+})\phi_e^{n,+}+W_e^{n+1/2}(\eta_q^{n+1,-})\phi_e^{n+1,-}\Big), \quad (22)\end{aligned}$$

with the free surface node index $q\in\mathcal{N}_F\cap\mathcal{N}_W$ and the wave maker node index $e\in\mathcal{N}_W$.

Combining all terms, we can express the discrete functional for the Miles variational formulation

(15) as

$$\begin{aligned}\mathcal{L}_h^t(\phi_h^t,\phi_{sh}^t,\eta_h^t,t) := &\sum_{n=1}^{N} M_{kl}^{n+1/2}(\phi_l^{n+1/2})(\eta_k^{n+1,-}-\eta_k^{n,+}) - \frac{1}{2}\Delta t_n(\phi_l^{n+1/2})(\eta_k^{n,+}+\eta_k^{n+1,-})D_{kl}^{n+1/2}\\ &-\frac{1}{2}\Delta t^n\Big(\mathcal{H}(\eta_k^{n,+},\phi_l^{n+1/2},\phi_{i'}^{n,+},t^{n+1/2})+\mathcal{H}(\eta_k^{n+1,-},\phi_l^{n+1/2},\phi_{i'}^{n+1,-},t^{n+1/2})\Big)\\ &-\frac{1}{2}\Delta t^n\Big(\big(W_q^{n+1/2}(\eta_q^{n,+})+W_q^{n+1/2}(\eta_q^{n+1,-})\big)\phi_q^{n+1/2}+\\ &\qquad W_e^{n+1/2}(\eta_q^{n,+})\phi_e^{n,+}+W_e^{n+1/2}(\eta_q^{n+1,-})\phi_e^{n+1,-}\Big)\\ &-(\eta_k^{n,-}-\eta_k^{n,+})(M_{kl}^n\phi_l^{n,+}),\end{aligned} \tag{23}$$

with the indices $i', j', e \in \mathcal{N}_{\Omega^n}$ and $k, l, q \in \mathcal{N}_F$.

3.3.1. Dynamics

The numerical approximation to the free surface gravity wave equations (9) can be obtained by applying the discrete variational principle $\delta\mathcal{L}_h^t = 0$ directly to the discrete Miles functional (15). Here the functional derivatives are defined as

$$\delta\mathcal{L}_h^t = \lim_{\epsilon\to 0}\frac{1}{\epsilon}\big(\mathcal{L}_h^t\big(\eta_h^t+\epsilon\delta\eta_h^t,\phi_h^t+\epsilon\delta\phi_h^t,\phi_{sh}^t+\epsilon\delta\phi_{sh}^t\big)-\mathcal{L}_h^t\big(\eta_h^t,\phi_h^t,\phi_{sh}^t\big)\big).$$

Taking the variations of (23) over the independent variables $\phi_l^{n+1/2}$, $\phi_l^{n,+}$, $\phi_{i'}^{n,+}$, $\phi_{i'}^{n+1,-}$, $\eta_k^{n,+}$, $\eta_k^{n+1,-}$ gives the dynamic equations for the nodal variables of the potential and wave height

$$\delta\phi_l^{n,+}: \quad M_{kl}^n\eta_k^{n,+} = M_{kl}^n\eta_k^{n,-}, \tag{24a}$$

$$\delta\phi_{i'}^{n,+}: \quad \frac{\partial\mathcal{H}(\eta_k^{n,+},\phi_l^{n+1/2},\phi_{i'}^{n,+},t^{n+1/2})}{\partial\phi_{i'}^{n,+}} = -W_e^{n+1/2}(\eta_q^{n,+}), \tag{24b}$$

$$\begin{aligned}\delta\eta_k^{n,+}: \quad &\Big(M_{kl}^{n+1/2}+\frac{\Delta t_n}{2}D_{kl}^{n+1/2}\Big)\phi_l^{n+1/2} = M_{kl}^n\phi_l^{n,+} - \frac{\Delta t^n}{2}\Big(\frac{\partial\mathcal{H}(\eta_k^{n,+},\phi_l^{n+1/2},\phi_{i'}^{n,+},t^{n+1/2})}{\partial\eta_k^{n,+}}\Big)\\ &-\frac{\Delta t^n}{2}\Big(\frac{\partial W_q^{n+1/2}(\eta_k^{n,+})}{\partial\eta_k^{n,+}}\phi_q^{n+1/2}+\frac{\partial W_e^{n+1/2}(\eta_k^{n,+})}{\partial\eta_k^{n,+}}\phi_e^{n,+}\Big),\end{aligned} \tag{24c}$$

$$\begin{aligned}\delta\phi_l^{n+1/2}: \quad &\Big(M_{kl}^{n+1/2}-\frac{\Delta t_n}{2}D_{kl}^{n+1/2}\Big)\eta_k^{n+1,-} = \Big(M_{kl}^{n+1/2}+\frac{\Delta t_n}{2}D_{kl}^{n+1/2}\Big)\eta_k^{n,+}\\ &+\frac{\Delta t^n}{2}\Big(\frac{\partial\mathcal{H}(\eta_k^{n,+},\phi_l^{n+1/2},\phi_{i'}^{n,+},t^{n+1/2})}{\partial\phi_l^{n+1/2}}+\frac{\partial\mathcal{H}(\eta_k^{n+1,-},\phi_l^{n+1/2},\phi_{i'}^{n+1,-},t^{n+1/2})}{\partial\phi_l^{n+1/2}}\Big)\\ &+\frac{\Delta t^n}{2}\Big(W_q^{n+1/2}(\eta_q^{n,+})+W_q^{n+1/2}(\eta_q^{n+1,-})\Big),\end{aligned} \tag{24d}$$

$$\delta\phi_{i'}^{n+1,-}: \quad \frac{\partial\mathcal{H}(\eta_k^{n+1,-},\phi_l^{n+1/2},\phi_{i'}^{n+1,-},t^{n+1/2})}{\partial\phi_{i'}^{n+1,-}} = -W_e^{n+1/2}(\eta_q^{n+1,-}), \tag{24e}$$

$$\delta\eta_k^{n+1,-}: \quad M_{kl}^{n+1}\phi_l^{n+1,+} = \Big(M_{kl}^{n+1/2} - \frac{\Delta t_n}{2}D_{kl}^{n+1/2}\Big)\phi_l^{n+1/2} - \frac{\Delta t^n}{2}\Big(\frac{\partial\mathcal{H}(\eta_k^{n+1,-},\phi_l^{n+1/2},\phi_{i'}^{n+1,-},t^{n+1/2})}{\partial\eta_k^{n+1,-}}\Big)$$
$$- \frac{\Delta t^n}{2}\Big(\frac{\partial W_q^{n+1/2}(\eta_k^{n+1,-})}{\partial\eta_k^{n+1,-}}\phi_q^{n+1/2} + \frac{\partial W_e^{n+1/2}(\eta_k^{n+1,-})}{\partial\eta_k^{n+1,-}}\phi_e^{n+1,-}\Big), \tag{24f}$$

with the indices $i', j' \in \mathcal{N}_{\Omega^n}$, $k, l, q \in \mathcal{N}_F$, $e \in \mathcal{N}_W$ and $q \in \mathcal{N}_F \cap \mathcal{N}_W$. In (24), we still need to define the variations of the Hamiltonian (19). The variations on the potential energy can be straightforwardly computed and are equal to

$$\delta(\frac{1}{2}gM_{kl}^{n+1/2}\eta_k^{n_p}\eta_l^{n_p}) = gM_{kl}^{n+1/2}\eta_k^{n_p}\delta\eta_l^{n_p}, \tag{25}$$

with $n_p = n, +$ or $n_p = n+1, -$. The variations of the kinetic energy with respect to the velocity potential include both variations of the velocity potential $\phi_{j'}$ and the free surface velocity potential ϕ_k, respectively, at interior nodes in the domain and at the free surface, resulting in

$$\delta(\frac{1}{2}A_{ij}^{n+1/2}(\eta^{n_p})\phi_i^{n_p}\phi_j^{n_p}) = (A_{lj'}^{n+1/2}(\eta^{n_p})\phi_l^{n+1/2} + A_{i'j'}^{n+1/2}(\eta^{n_p})\phi_{i'}^{n_p})\delta\phi_{j'}^{n_p}$$
$$+ (A_{lk}^{n+1/2}(\eta^{n_p})\phi_l^{n+1/2} + A_{i'k}^{n+1/2}(\eta^{n_p})\phi_{i'}^{n_p})\delta\phi_k^{n+1/2}. \tag{26}$$

The variations of the kinetic energy with respect to the free surface elevation η_l are more complicated to compute since the nodal coordinates (x_i, z_i) in the mesh change every time step due the free surface and piston wave maker movement. By introducing

$$C_{sij}^{n+1/2} = \frac{\partial A_{ij}^{n+1/2}}{\partial z_b}\frac{\partial z_b}{\partial\eta_s^{n_p}}, \tag{27}$$

we can compute the variations of the kinetic energy with respect to the free surface elevation

$$\delta_{\eta_s}(\frac{1}{2}A_{ij}^{n+1/2}\phi_i^{n_p}\phi_j^{n_p}) = \frac{1}{2}C_{si'j'}^{n+1/2}\phi_{i'}^{n_p}\phi_{j'}^{n_p}\delta\eta_s^{n_p} + \frac{1}{2}C_{slj'}^{n+1/2}\phi_l^{n+1/2}\phi_{j'}^{n_p}\delta\eta_s^{n_p}$$
$$+ \frac{1}{2}C_{si'k}^{n+1/2}\phi_{i'}^{n_p}\phi_k^{n+1/2}\delta\eta_s^{n_p} + \frac{1}{2}C_{slk}^{n+1/2}\phi_l^{n+1/2}\phi_k^{n+1/2}\delta\eta_s^{n_p}.$$

Finally, the variations on the Hamiltonian can be written as

$$\delta\mathcal{H}_h^{n_p}(\phi_i^{n_p},\eta_s^{n_p}) = (A_{lj'}^{n+1/2}(\eta^{n_p})\phi_l^{n+1/2} + A_{i'j'}^{n+1/2}(\eta^{n_p})\phi_{i'}^{n_p})\delta\phi_{j'}^{n_p}$$
$$+ (A_{lk}^{n+1/2}(\eta^{n_p})\phi_l^{n+1/2} + A_{i'k}^{n+1/2}(\eta^{n_p})\phi_{i'}^{n_p})\delta\phi_k^{n+1/2}$$
$$+ \Big(\frac{1}{2}C_{si'j'}^{n+1/2}\phi_{i'}^{n_p}\phi_{j'}^{n_p} + \frac{1}{2}C_{slj'}^{n+1/2}\phi_l^{n+1/2}\phi_{j'}^{n_p}$$
$$+ \frac{1}{2}C_{si'k}^{n+1/2}\phi_{i'}^{n_p}\phi_k^{n+1/2} + \frac{1}{2}C_{slk}^{n+1/2}\phi_l^{n+1/2}\phi_k^{n+1/2} + gM_{ks}^{n+1/2}\eta_k^{n_p}\Big)\delta\eta_l^{n_p}. \tag{28}$$

Variations of the wave maker contribution in the Miles functional with respect to the free surface

elevation can be computed analogously, resulting in

$$\begin{aligned}\delta\big(W_m^{n+1/2}(\eta_k^{n_p})\phi_m^{n_p}\big) &= \frac{\partial W_k^{n+1/2}(\eta_k^{n_p})}{\partial \eta_k^{n_p}}\phi_k^{n+1/2}\delta\eta_k^{n_p} + \frac{\partial W_m^{n+1/2}(\eta_k^{n_p})}{\partial \eta_k^{n_p}}\phi_m^{n_p}\delta\eta_k^{n_p} \\ &= B_k^{n+1/2}(\eta_k^{n_p})\phi_k^{n+1/2}\delta\eta_k^{n_p} + B_m^{n+1/2}(\eta_k^{n_p})\phi_m^{n_p}\delta\eta_k^{n_p}, \end{aligned} \tag{29}$$

with $B_m(\eta_k^{n_p}) := \frac{\partial W_m(\eta_k^{n_p})}{\partial \eta_k^{n_p}}$. As we can see in (24), there is no dynamical equation for the velocity potential $\phi_{j'}$ at the nodes in the domain Ω^n. We can rename therefore the interior potentials as $\phi_{j'}^n := \phi_{j'}^{n,+}$ and $\phi_{j'}^{n+1} := \phi_{j'}^{n+1,-}$. Due to (24a) we obtain then that the wave height η is continuous in time, and denote $\eta_k^n := \eta_k^{n,+}$ and $\eta_k^{n+1} := \eta_k^{n+1,-}$. Also we can rename $\phi_l^{n,+}$ as ϕ_l^n.

Introducing the variations (28) of the Hamiltonian and the variations (29) of the wave maker term into (24), the final system of discrete equations for the potential and wave height becomes equal to

$$\begin{cases} \Big(M_{kl}^{n+1/2} + \frac{\Delta t_n}{2}D_{kl}^{n+1/2}\Big)\phi_l^{n+1/2} = M_{kl}^n\phi_l^n - \frac{\Delta t^n}{2}\Big(\frac{1}{2}C_{si'j'}^{n+1/2}\phi_{i'}^n\phi_{j'}^n + \frac{1}{2}C_{slj'}^{n+1/2}\phi_l^{n+1/2}\phi_{j'}^n \\ \qquad\qquad + \frac{1}{2}C_{si'k}^{n+1/2}\phi_{i'}^n\phi_k^{n+1/2} + \frac{1}{2}C_{slk}^{n+1/2}\phi_l^{n+1/2}\phi_k^{n+1/2} + gM_{ks}^{n+1/2}\eta_k^n\Big) \\ \qquad\qquad - \frac{\Delta t^n}{2}\Big(B_q^{n+1/2}(\eta_q^n)\phi_q^{n+1/2} + B_e^{n+1/2}(\eta_q^n)\phi_e^n\Big), \\ A_{i'j'}^{n+1/2}(\eta_k^n)\phi_{j'}^n + A_{i'l}^{n+1/2}(\eta_l^n)\phi_l^{n+1/2} = -W_e^{n+1/2}(\eta_e^n), \end{cases}$$

$$\begin{cases} \Big(M_{kl}^{n+1/2} - \frac{\Delta t_n}{2}D_{kl}^{n+1/2}\Big)\eta_k^{n+1} = \Big(M_{kl}^{n+1/2} + \frac{\Delta t_n}{2}D_{kl}^{n+1/2}\Big)\eta_k^n + \frac{\Delta t^n}{2}\Big(W_q^{n+1/2}(\eta_q^n) + W_q^{n+1/2}(\eta_q^{n+1})\Big) \\ \qquad\qquad + \frac{\Delta t^n}{2}\Big(A_{lk}^{n+1/2}(\eta_k^n)\phi_l^{n+1/2} + A_{i'k}^{n+1/2}(\eta_k^n)\phi_{i'}^n + \\ \qquad\qquad\qquad A_{lk}^{n+1/2}(\eta_k^{n+1})\phi_l^{n+1/2} + A_{i'k}^{n+1/2}(\eta_k^{n+1})\phi_{i'}^{n+1}\Big), \\ A_{i'j'}^{n+1/2}(\eta_k^{n+1})\phi_{j'}^{n+1} + A_{i'l}^{n+1/2}(\eta_l^{n+1})\phi_l^{n+1/2} = -W_e^{n+1/2}(\eta_e^{n+1}), \end{cases}$$

$$\begin{aligned} M_{kl}^{n+1}\phi_l^{n+1} &= \Big(M_{kl}^{n+1/2} - \frac{\Delta t_n}{2}D_{kl}^{n+1/2}\Big)\phi_l^{n+1/2} - \frac{\Delta t^n}{2}\Big(\frac{1}{2}C_{si'j'}^{n+1/2}\phi_{i'}^{n+1}\phi_{j'}^{n+1} + \frac{1}{2}C_{slj'}^{n+1/2}\phi_l^{n+1/2}\phi_{j'}^{n+1} \\ &+ \frac{1}{2}C_{si'k}^{n+1/2}\phi_{i'}^{n+1}\phi_k^{n+1/2} + \frac{1}{2}C_{slk}^{n+1/2}\phi_l^{n+1/2}\phi_k^{n+1/2} + gM_{ks}^{n+1/2}\eta_k^{n+1}\Big) \\ &- \frac{\Delta t^n}{2}\Big(B_q^{n+1/2}(\eta_q^{n+1})\phi_q^{n+1/2} + B_e^{n+1/2}(\eta_q^{n+1})\phi_e^{n+1}\Big). \end{aligned} \tag{30}$$

The first and second step, indicated by curly brackets, are implicit in time, the third step is explicit, which is analogous to the Stormer-Verlet scheme. If we consider the wave basin without the wave maker, we have no time dependency of the matrices and the wave maker terms vanish. In this case we can easily show the analogy of the time scheme for the potential flow, which has a Hamiltonian structure, and the symplectic Stormer-Verlet integration scheme for the harmonic oscillator as given in [13]. This observation motivated the choices made in the approximation of the free surface potential in (13) and the mixed quadrature rule for the time integral of the Hamiltonian in (20). The

Stormer-Verlet type integration scheme described in this section is an extension of the symplectic Euler scheme for the nonlinear water wave equations without a wave maker that we described in [8].

4. Numerical Results

4.1. Verification

4.1.1. Nonlinear Fenton waves

We first verify our variational finite element method against a nonlinear exact solution of the free surface water wave equations using Fenton's method. In this technique a Fourier approximation of the velocity potential and wave height is used at discrete points in a two-dimensional domain with a flat bottom and periodic boundary conditions in the horizontal. The resulting wave solution is a harmonic wave that travels undisturbed.

We initialize the numerical simulation with the harmonic Fenton wave solution and simulate for 100 time periods on a mesh with 128×16 elements, with evenly distributed points in the horizontal and vertical direction. The numerical simulation shows no decay in the wave amplitude, even after 100 time periods, indicating discrete energy conservation, which is confirmed by Fig. 3. A phase shift in the final wave profile can, however, be observed when compared with the initial wave profile, which is caused by the dispersion error present in the numerical scheme. We also performed a series

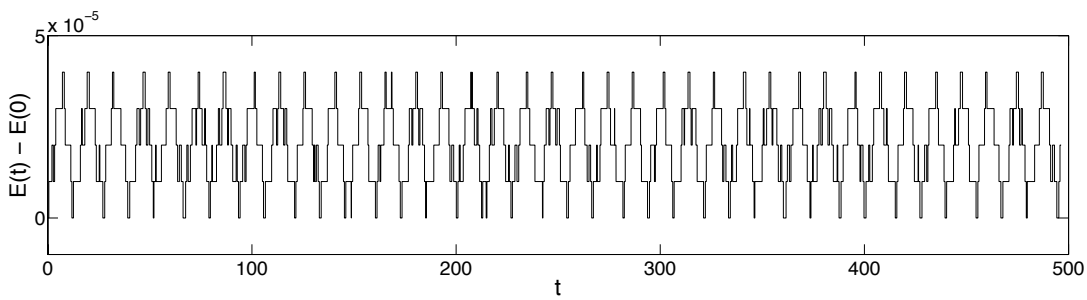

Figure 3: Plot of discrete energy difference $E(t) - E(0)$ versus time t, where $E(t)$ is the discrete energy at a given time t. The discrete energy has bounded fluctuations in time, but the average remains constant.

of tests on various meshes in order to verify numerically the order of convergence of the variational finite element discretization. The results are presented in Table 1. Here it is necessary to mention, that the exact solution for the velocity potential is determined up to an arbitrary constant. This arbitrary constant needs to be removed in order to compute the correct order of convergence, which is done by considering the solution of the velocity potential at two time levels.

4.2. Validation against laboratory data

We now validate the numerical scheme with experimental data provided by the Maritime Research Institute Netherlands (MARIN). The experimental data consist of recordings of wave height measurements using probes at specific locations in the wave basin. There are two experimental setups: the first case concerns several irregular long crested waves, which are propagating over a sloping bottom, and the second test case concerns several wave groups over a flat bottom, see

Table 2. In both cases, a piston type wave maker at the left side of the domain and a beach at the right side of the domain are installed. Consequently, while the piston type wave maker generates waves travelling towards the right, the beach reduces the incoming wave reflections by damping them via bore formations. Our present numerical scheme does not, however, accommodate a beach and therefore, a solid wall is introduced instead. This limits us to conduct numerical simulations till the reflected incoming waves interfere with the numerical results taken at the given probe locations. We investigate the capabilities of the numerical method to deal with (i) a sloping bottom; (ii) waves generated by the irregular movement of the wave maker; and (iii) wave focussing.

4.2.1. Irregular waves propagating over a sloping bottom

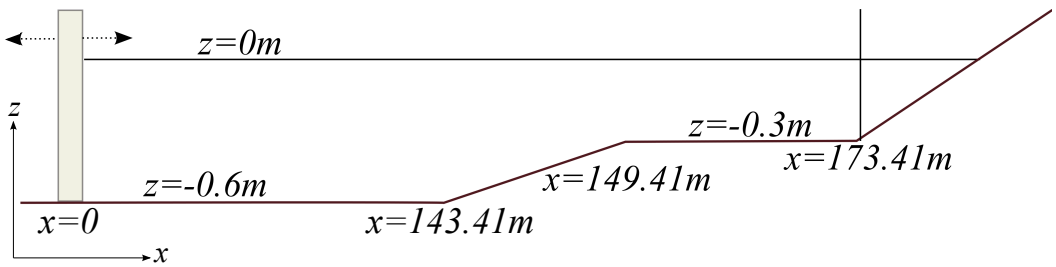

Figure 4: Sketch of bathymetry of the wave basin for Case 1, see Table 2.

First, we show a sketch of the bathymetry of the wave basin in Fig. 4. A piston-type wave maker is placed at the left boundary of the domain. The wave maker always starts from rest at $x = 0m$ and can only translate in the horizontal direction. To the right of the wave maker there is a flat bottom with water depth of $0.60m$. At $x = 143.41m$ a slope with steepness of 1:20 starts. It ends at $x = 149.41m$ from the wave generator at a water depth of $0.30m$. Behind the slope there is a $24m$ long flat bottom part. A sloping beach starts at $x = 173.41m$ from the wave generator. As mentioned, in the numerical simulations the sloping beach is replaced with a vertical wall at $x = 173.41m$.

Table 1: Error in space in the L^2 and L^∞ - norms, and order of accuracy and deviation of total energy for Fenton waves. Wave height and potential are, respectively, η and ϕ. Time $t = 10T_{per} = 49.636s$, $\Delta t = 0.01551125s$, $\Delta x = 0.1551121m$, $\Delta z = 0.25m$, uniform distribution of points in the vertical direction.

		L^2		L^∞		Energy deviation	
Mesh size		L^2-error	order	C-error	order	ΔE	order
$\Delta x,\ \Delta z,\ \Delta t$	η	0.052831	–	0.0365923	–	7.E-4	–
	$\Delta\phi$	0.0045161	–	0.0054115	–		
$\frac{\Delta x}{2},\ \frac{\Delta z}{2},\ \frac{\Delta t}{2}$	η	0.131235	2.009	0.00900984	2.022	1.7E-4	2.042
	$\Delta\phi$	0.0007522	2.586	0.00118985	2.185		
$\frac{\Delta x}{4},\ \frac{\Delta x}{4},\ \frac{\Delta t}{4}$	η	0.00327116	2.004	0.00223324	2.012	4.0E-5	2.087
	$\Delta\phi$	6.2E-5	3.601	0.00024878	2.258		
$\frac{\Delta x}{8},\ \frac{\Delta x}{8},\ \frac{\Delta t}{8}$	η	0.00081288	2.009	0.000554157	2.011	1.0E-5	2.0
	$\Delta\phi$	5.68E-6	3.448	6.418E-5	1.955		

Table 2: Test cases.

Case 1	variable bottom	Run 102003	blind case
		Run 103001	open case
		Run 104001	blind case
Case 2	flat bottom	Run 202002	open case
		Run 203001	blind case
		Run 204001	blind case

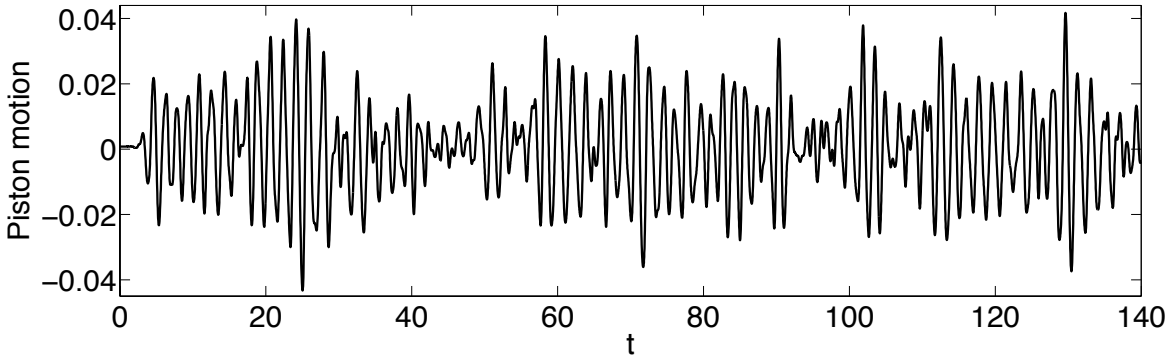

Figure 5: Piston motion for Run 103001.

Table 3: Locations of wave probes for wave height measurements for Run 103001.

Wave probe number	1	2	9	12	13	15	17	25
Distance (m)	39.15	78.80	102.12	143.41	146.43	149.41	157.74	172.89

The piston motion, velocity and acceleration in the experiments were provided for the numerical simulations, see Fig. 5. A positive piston motion corresponds to a movement into the basin. The wave elevations are measured at various probes, see in Table 3 for an overview of the positions. Experimental data for the variable bottom wave basin are provided for three test runs, which are numbered as Runs 102003, 103001 and 104001. Run 103001 is an open case for which measurements at all probes are provided. The remaining runs are blind cases for which measurements are given only at Probe 1. Therefore we only consider the open test case – Run 103001 since this case provides the largest amount of data. The results of the validation computations for the variable bottom can be summarized as:

Run 103001: For this test case the wave maker movement shown in Fig. 5 generates highly irregular waves. A fixed time step $\Delta t = 0.00125s$ is used in the numerical simulations. In the horizontal direction there are $N_x = 12000$ equidistantly distributed points. In the vertical direction we have $N_z = 10$ points distributed exponentially, such that the smallest element size is obtained near the free surface.

A comparison of the experiments and numerical simulations at all available probes is shown in Fig. 6. The experimental ("red") and numerical results ("blue") agree well. This agreement could be further improved by using variable time stepping criteria that preserve the accuracy in the wave speed for the waves with different wave length generated by the wave maker.

Since the incoming waves reach the solid wall around $t = 110s$, comparisons with experimental data have been made only till $t = 120s$. This in order to prevent that reflections from the artificial solid wall pollute the simulations. As can be seen for Probe 25 at $x = 172.89m$, which is located close to the reflecting boundary, the comparison stops to be adequate after $t = 110s$. To obtain a rough estimate when the reflected waves will reach the probe, we use the linear frequency relation for an intermediate water depth $\omega^2 = gk\tanh(kH_0)$, with $H_0 = 0.6m$. As we can see from Figure 7(a), there is a large number of long waves with frequencies around $\omega = 3/s$. The corresponding wavenumber is $k = 1.362/m$. For an average depth $H_0 = 0.6m$, we obtain a velocity $c_p = 2.42m/s$. The distance of $173.41m$ will then be covered in 94.7 seconds by the fastest waves, which seems to be an adequate estimate for the time to stop the numerical simulations before they are polluted too much by reflections from the end wall.

As another verification of our numerical results, we compute spectra using a fast Fourier transform (FFT) to analyze the data from the numerical simulation and the laboratory experiment. We consider two probes: Probe 1 at $x = 39.15m$ located at the beginning of the basin; Probe 9 at $x = 102.12m$ in the centre. We can observe in Fig. 7 that the comparison is good for Probes 1 and 9.

The spectral analysis is also useful before the numerical simulation is performed to estimate the necessary mesh size and time step. Considering the spectra of the laboratory data at the first probe ("red"), see Fig. 7(a), we see that frequencies up to $\omega = 11/s$ are relevant, the rest can be neglected. After an analysis of the wave heights at all the probes, we stay on the safe side by taking a limiting frequency $\omega = 15/s$. The time period of the shortest wave is then $T = 2\pi/\omega = 0.419s$. Taking at least 10 time steps per period, we obtain a minimal time step $\Delta t = 0.0419s$. Using the linear frequency relation for the intermediate depth H_0, we find the

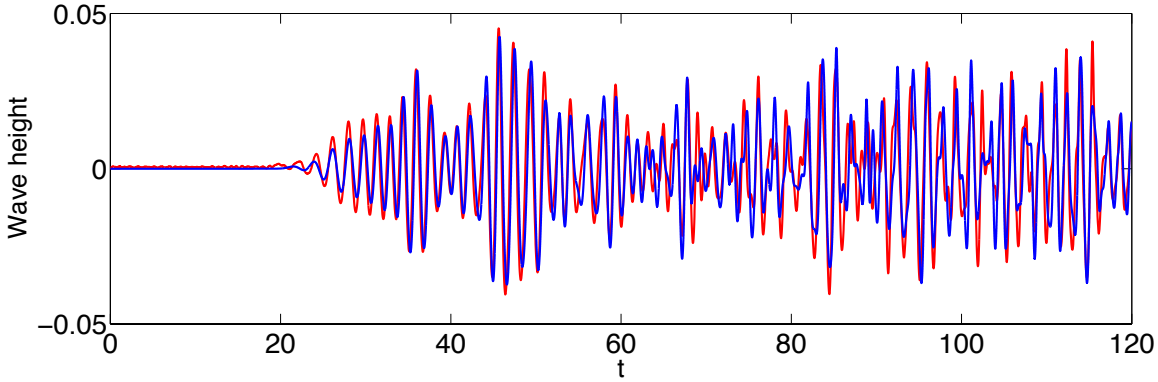

(a) $x = 39.15m$.

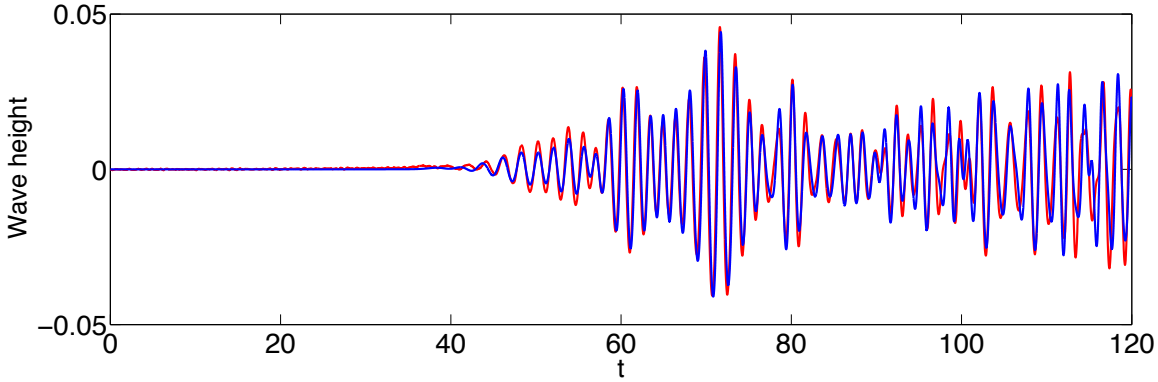

(b) $x = 78.80m$.

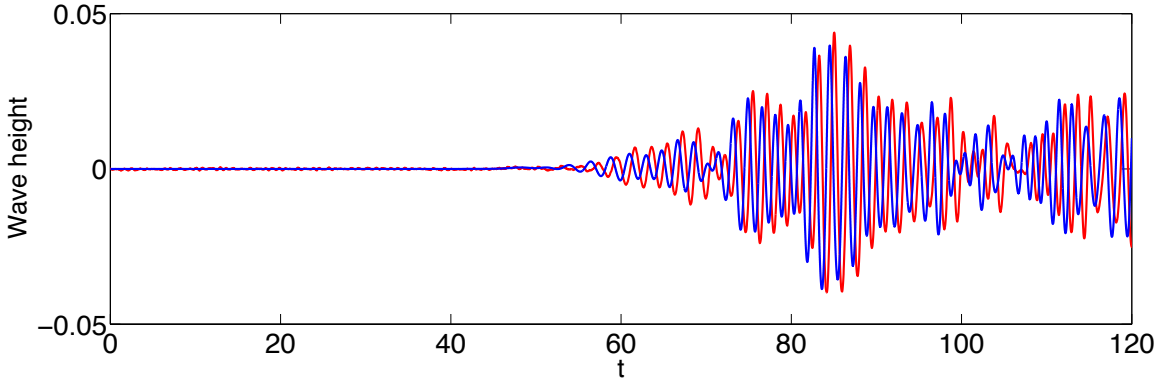

(c) $x = 102.12m$.

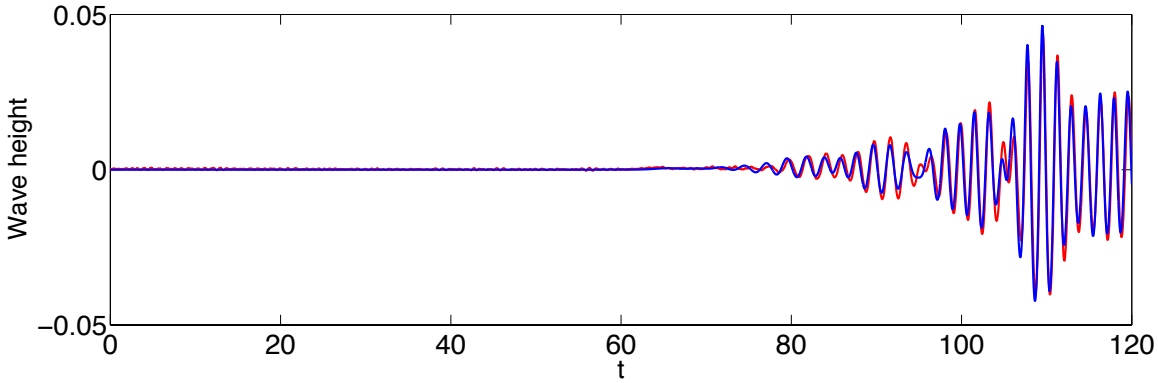

(a) $x = 143.41m$.

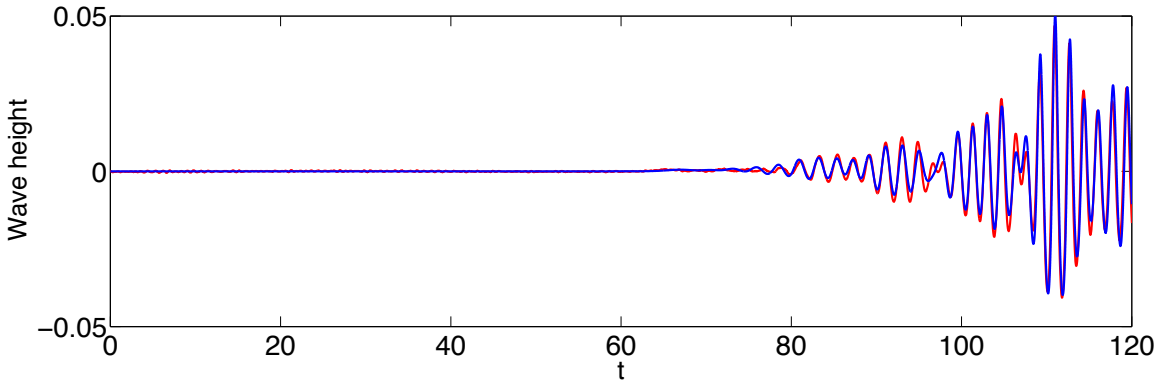

(b) $x = 146.43m$.

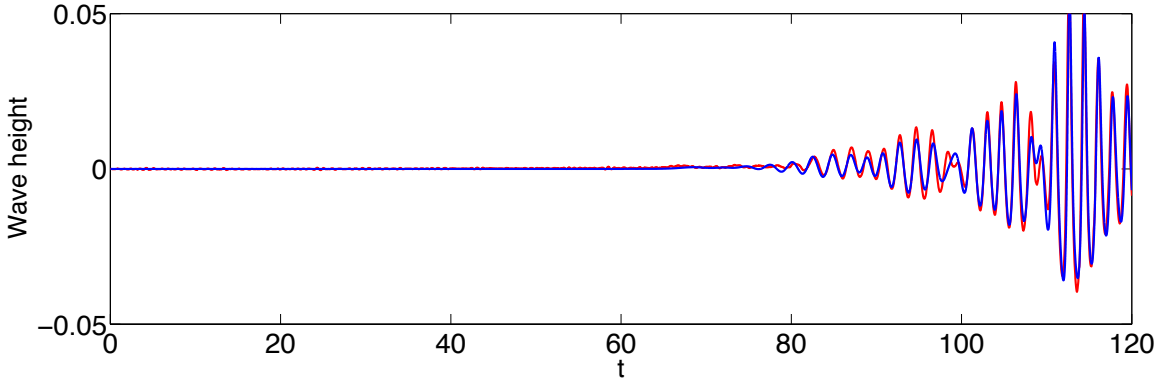

(c) $x = 149.41m$.

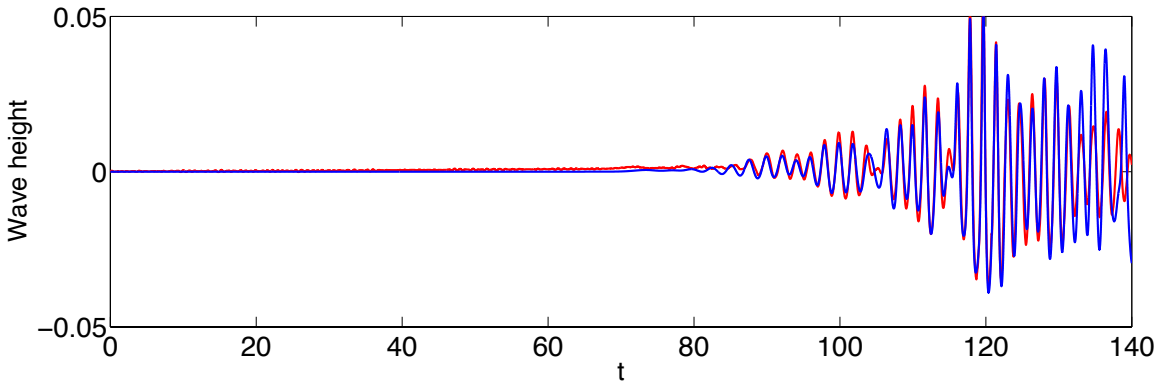

(a) $x = 157.74m$.

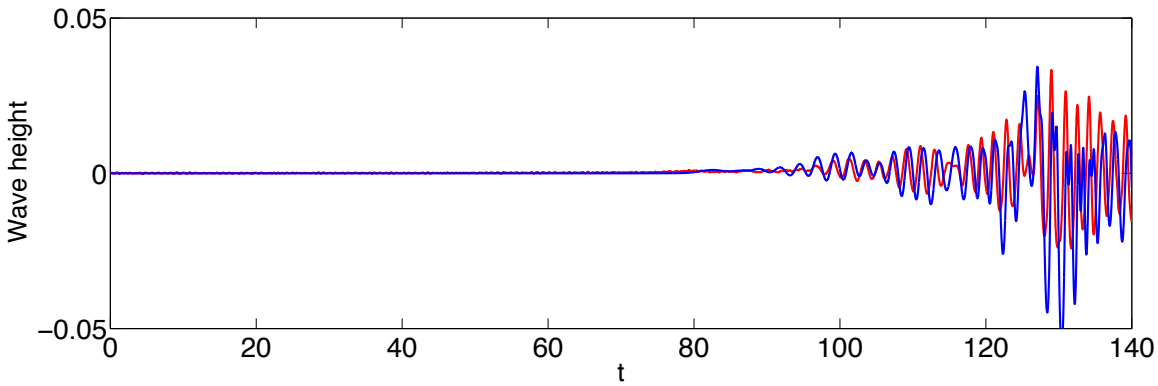

(b) $x = 172.89m$.

Figure 6: Comparison of wave heights in experiments and numerical simulation for the test case with a sloping bottom (Run 103001) at all available probe locations. The numerical simulation is performed on a mesh of 12000×10 elements with time step $\Delta t = 0.00125s$. Experiments are in "red" and numerical simulations in "blue".

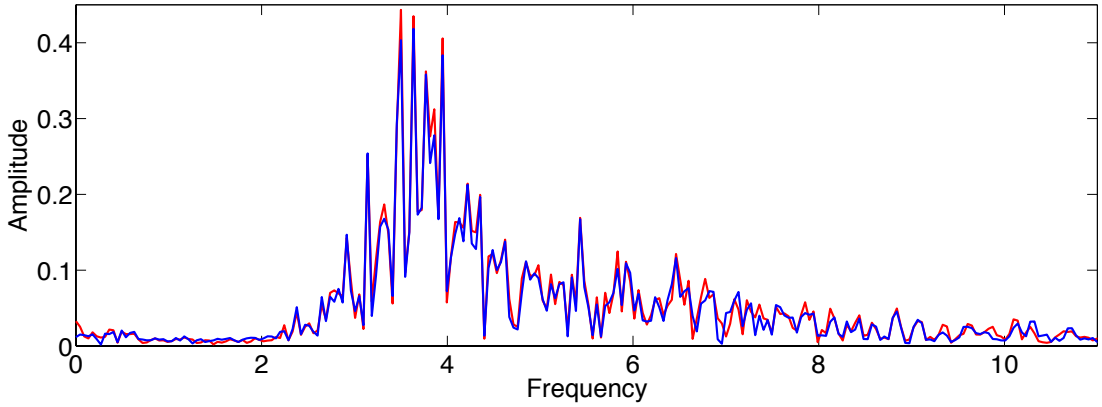

(a) $x = 39.15m$.

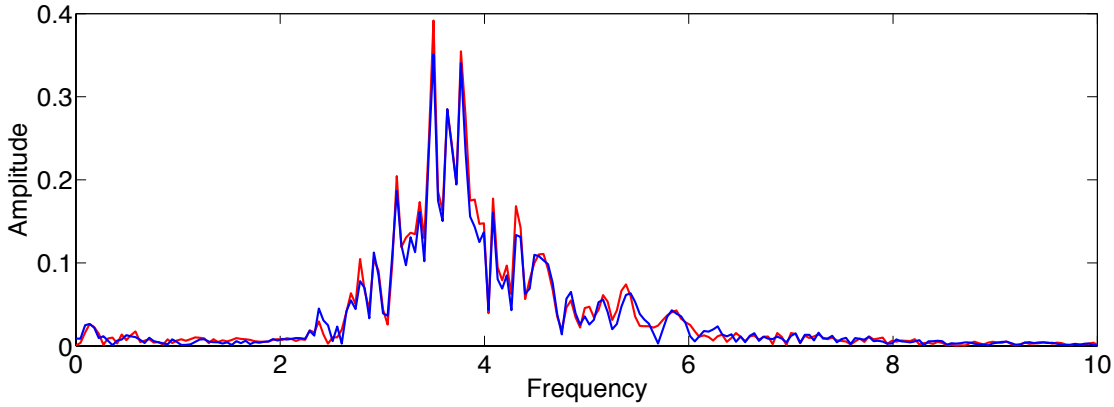

(b) $x = 102.12m$.

Figure 7: Spectra of measured wave height ("red") and computed wave height ("blue") at Probes 1 and 9.

Table 4: Location of wave probes for wave height measurements for Run 202002.

Wave probe number	1	2	3	4	5	6
Distance (m)	10	20	40	49.5	50	54

corresponding wavenumber $k = 22.94/m = 2\pi/\lambda$. Taking at least 10 points per shortest wave length $\lambda = 0.274m$ we obtain that the required horizontal mesh size is $\Delta x = 0.0274m$, which gives a number of elements equal to $N_x = 173.41/\Delta x \approx 6500$.

4.2.2. Wave groups propagating over a flat bottom

In this test case, the wave basin has a flat bottom and the horizontally-driven wave maker always starts from rest at $x = 0m$. The wave basin is $1m$ deep and $195.4m$ long. The piston motion, velocity and acceleration measured in the experiments are shown in Fig. 9. The wave elevations are measured at various probes, see Table. 4 for the locations. Experimental data from the wave basin are provided for three test runs, which are numbered as Runs 202002, 203001 and 204001, see Table 2. Run 202002 is an open case for which measurements at all probes are provided. The remaining runs are blind cases for which measurements are given at Probe 1 only. Therefore we limit the comparison to the open test case – Run 202002. We can draw the following conclusions from the comparison between the experiments and numerical simulations:

Run 202002: The measured and computed wave heights at the probes are in good agreement, see Fig. 10. Several snapshots of the numerical simulation are presented in Fig. 10. It can be clearly seen that the piston incidents a slow moving wave group followed by a fast moving wave group, resulting in wave focussing at around $t = 109.56s$.

The spectral analysis is used again to define the necessary mesh size and time step. We analyzed the laboratory data for all available probes. Considering the spectrum of the second probe ("red") placed at $x = 20m$, see Figure 10(a), we see that the frequencies up to $\omega = 11/s$ are dominant, the rest we can neglect. This limiting frequency corresponds to a time period $T = 2\pi/\omega = 0.571s$. Taking 10 time steps per period, we have the minimal time step $\Delta t = 0.0571s$. Using the linear frequency relation for the intermediate water depth $\omega^2 = gk\tanh(kH_0)$, where the depth $H_0 = 1m$, we find the corresponding wavenumber $k = 12.34/m = 2\pi/\lambda$. Taking at least 10 points per shortest wave length $\lambda = 0.509m$ we have the required horizontal mesh size of $\Delta x = 0.0509m$. Considering the experimental spectra of the fifth probe, placed at $x = 50m$ (shown in "red" in Figure 10(b)), we see a peak at $\omega = 35/s$. We know from the laboratory experiment that a splash occurs around this probe, therefore special attention should be given to this region. For the limiting frequency $\omega = 36/s$ the time period of the shortest wave is $T = 0.1745s$ and the wave length is $\lambda = 0.0385m$. The required time step is then estimated as $\Delta t = 0.01745s$ and the mesh size is $\Delta x = 0.00385m$. The mesh size should be much smaller near the fifth probe than near the first probe.

To save the computing time we adapt the mesh to satisfy the mesh size requirements around each probe. At beginning of the domain $\Delta x = 0.0509m$ is sufficient, but in the splash area around $x = 50.5m$ we require at least $\Delta x = 0.00385m$. The parameters for the calculations are selected as: $\Delta x = 0.01559m$ at the beginning of the domain, $\Delta x = 0.0027m$ in the splash zone.

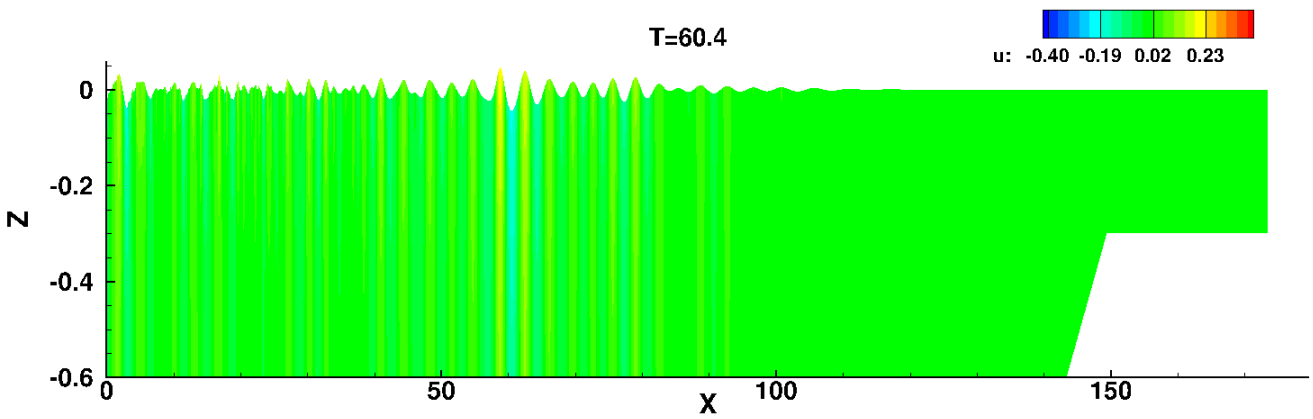

(a)

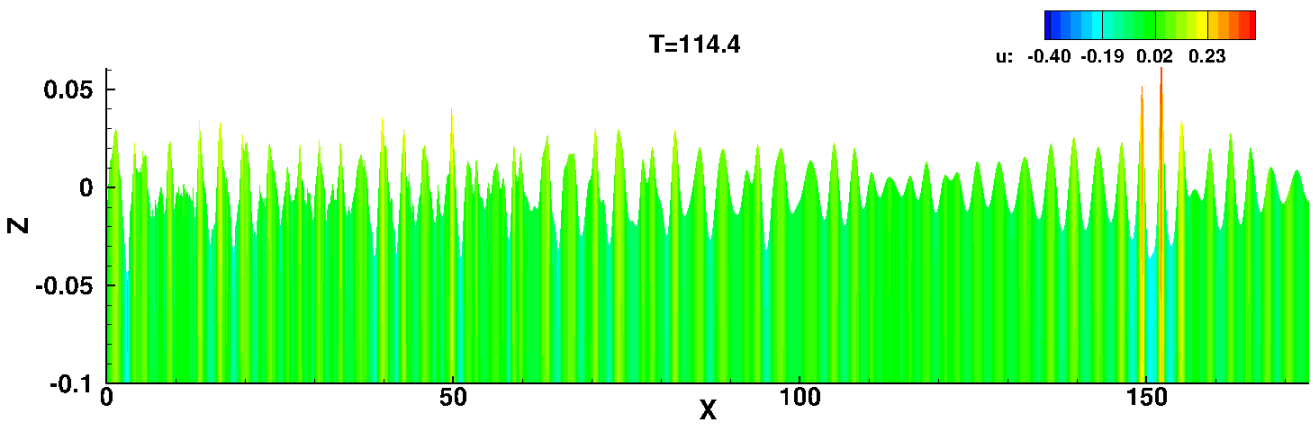

(b)

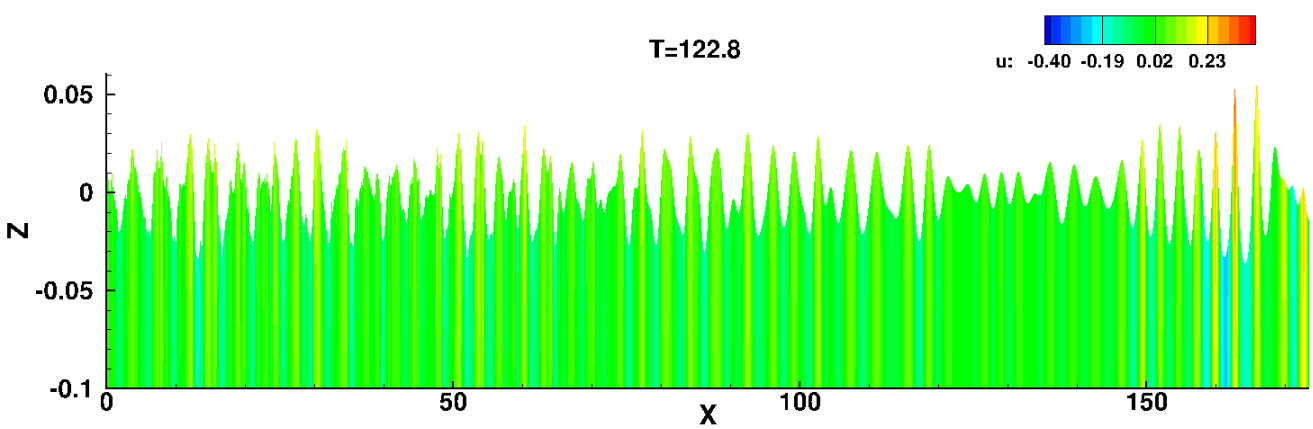

(c)

Figure 8: Snapshots of numerical simulations at times $t = 60.4s$, $t = 114.4s$ and $t = 122.8s$ for the variable bottom test case (Run 103001). Observe the highly irregular waves generated by the wave maker and the reflections due to a solid wall at the right end of the domain. The numerical simulations were performed on a 12000×10 mesh with time step $\Delta t = 0.00125s$. In Fig. 9(a) we show the complete domain, Figures 9(b) and 9(c) are zoomed in near the free surface.

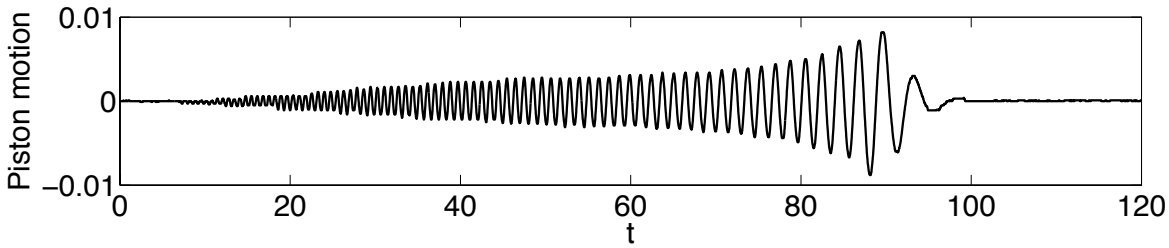

Figure 9: Piston motion for Run 202002.

The time step is constant $\Delta t = 0.0005s$. As we can see for the second probe in Fig. 10(a), the comparison between the experimental spectra ("red") and those of the numerical simulation ("blue") is good. Unfortunately, for the fifth probe, see Fig. 10(b), we do not capture in the numerical simulations the peak at $\omega = 35/s$ in the experimental spectra. The origin of this peak at $\omega = 35/s$ in the experiments is, however, unclear.

5. Conclusions

A new variational finite element method is presented to compute the dynamics of nonlinear free surface potential flow water waves. It is based on a numerical discretization of Miles' variational principle together with a space-time approach. To obey the geometrical conservation law, we derived the discretization directly in space-time using polynomial basis functions that are continuous in space, but discontinuous in time. The numerical discretization is equivalent to a combination of a second order finite element discretization in space and second order symplectic Stormer-Verlet discretization in time. We use a Newton method to solve the nonlinear algebraic system in combination with the iterative linear solvers available in the PETSc package. The PETSc package gives a good performance relative to other methods, such as direct solvers and locally build and optimized conjugate gradient solvers. We found that preallocation of memory for the matrix storage rather than a dynamic memory allocation improves the performance of the package substantially. An extra advantage of PETSc is that parallelization is a built-in feature.

Verification of the numerical discretization against harmonic Fenton waves for 100 time periods demonstrated the accuracy, efficiency and robustness of the novel variational finite element method in simulating waves for a long time. A key advantage of this finite element discretization is that the discrete energy is conserved in time and thus, there is no reduction in wave height due to numerical dissipation. The numerical discretization has, however, a small dispersion error which can be further reduced by using a higher order accurate finite element discretization. Validation of the numerical method with experimental data reveals that the agreement is good. Furthermore, the numerical scheme is capable of producing the wave focussing phenomena observed in the experiments very accurately. For highly irregular propagating waves the accuracy can be further improved by using an adjustable time step.

The numerical validation with the MARIN experiments was somewhat limited because of the lack of proper absorbing boundary conditions at the beach. An interesting approach to this problem is to couple the variational numerical method for nonlinear potential flow water waves with a discretization of the shallow water equations near the beach via interface conditions. The bore

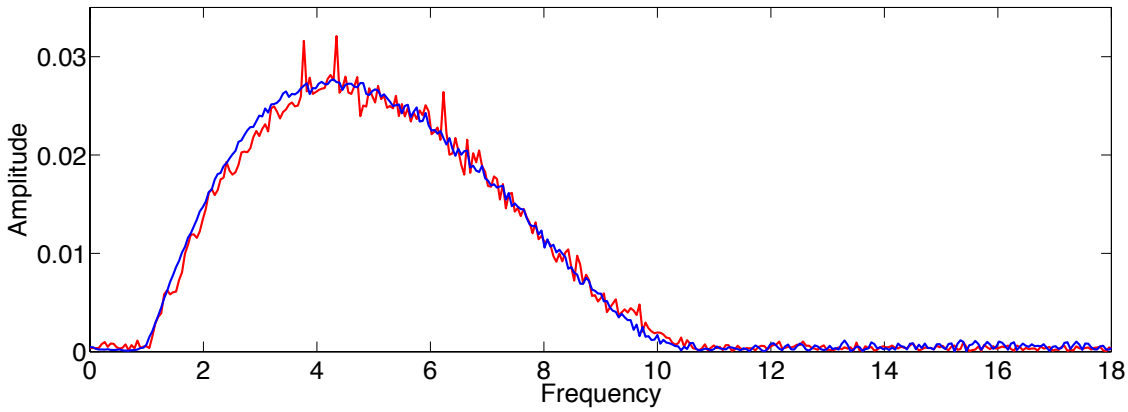

(a) $x = 20m$.

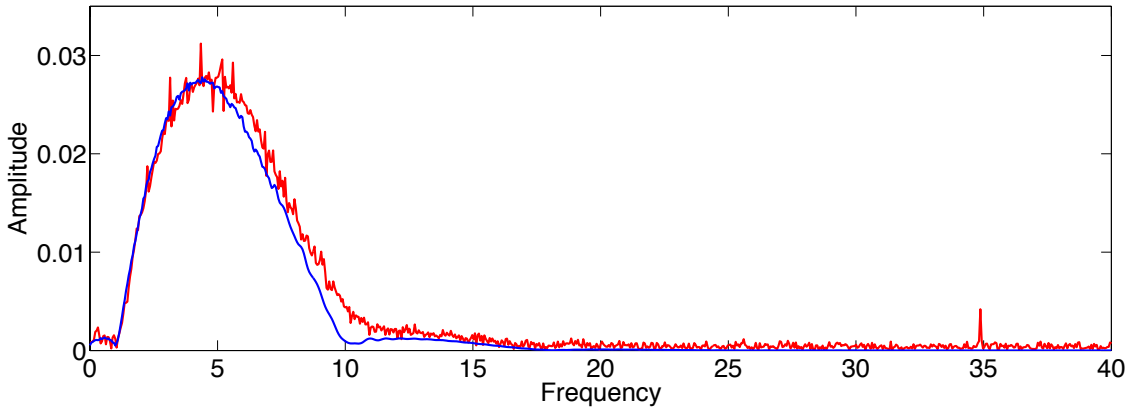

(b) $x = 50m$.

Figure 10: Spectra of measured wave height ("red") and computed wave height ("blue") for Run 202002 at Probes 2 and 5.

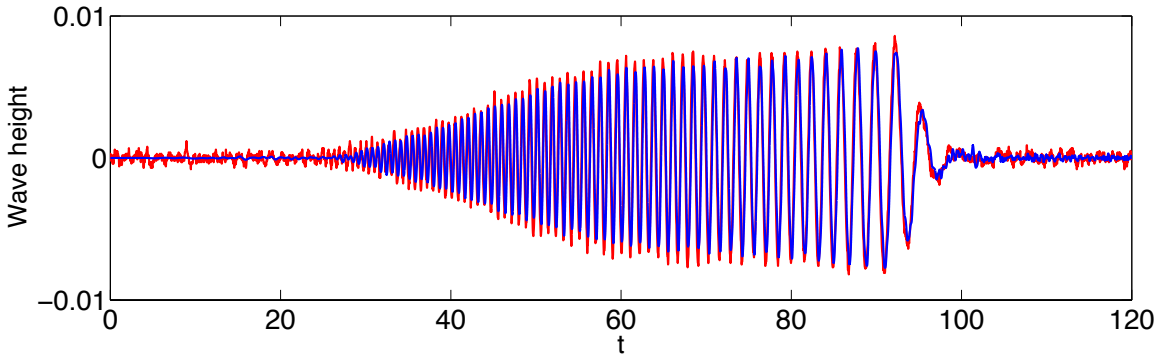

(a) $x = 10m$.

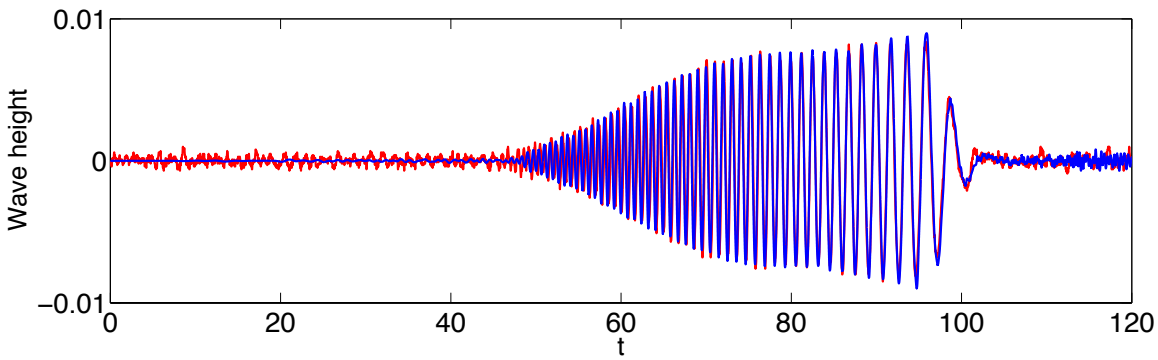

(b) $x = 20m$.

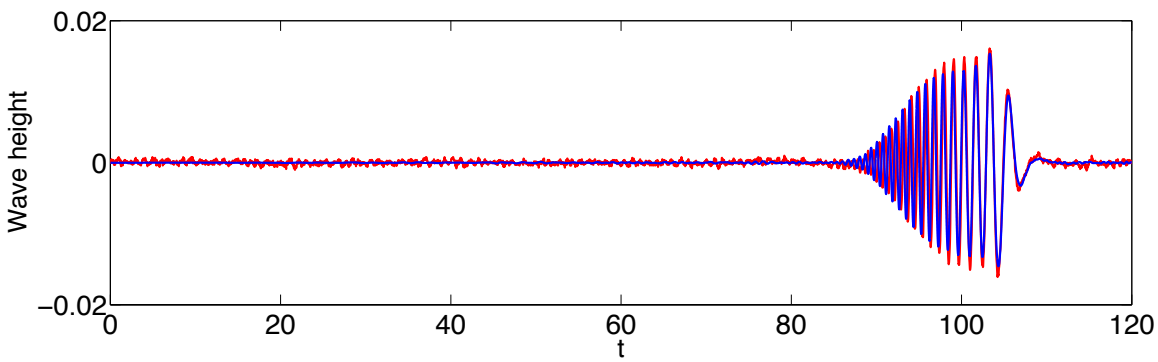

(c) $x = 40m$.

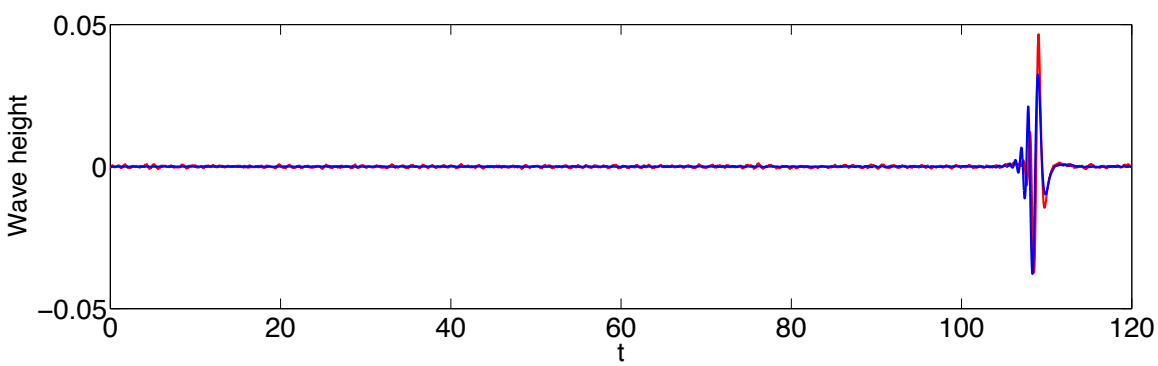

(d) $x = 49.5m$.

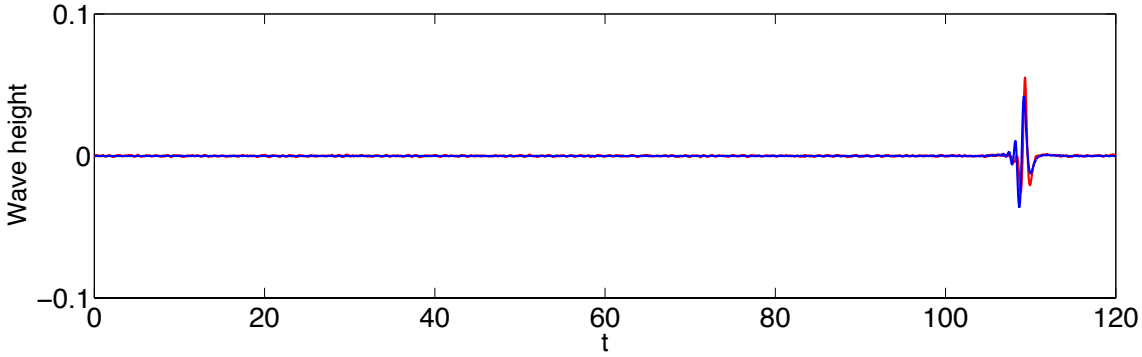

(e) $x = 50m$.

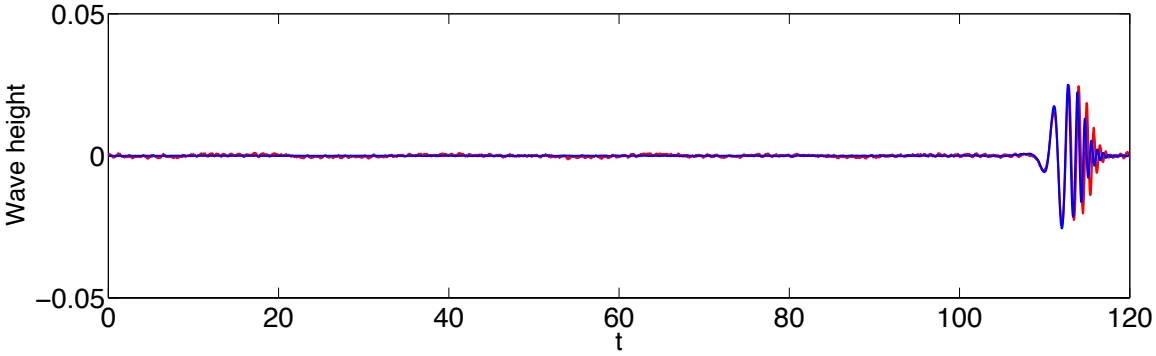

(f) $x = 54m$.

Figure 10: Comparison of wave heights in experiments and numerical simulations for the test case with a flat bottom (Run 202002) at all available probe locations. The numerical simulation is performed on a nonuniform stencil with 6000×10 elements with time step $\Delta t = 0.0005s$. Experiments are in "red" and numerical simulations in "blue".

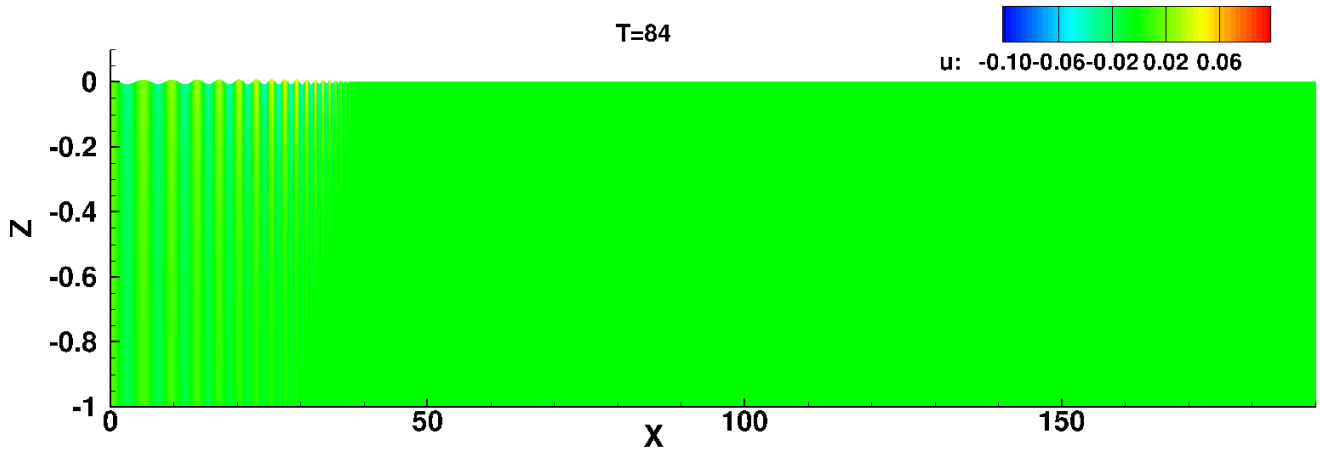
T=84
u: -0.10-0.06-0.02 0.02 0.06
0
-0.2
-0.4
-0.6
-0.8
-1
Z
0
50
100
150
X

(a)

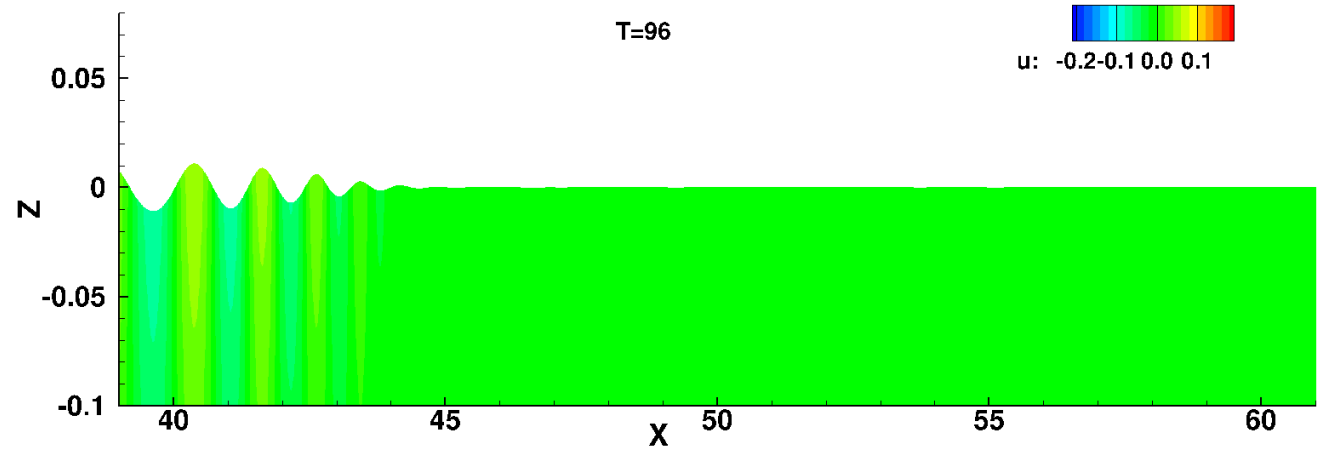
T=96
u: -0.2-0.1 0.0 0.1
0.05
0
-0.05
-0.1
Z
40
45
50
55
60
X

(b)

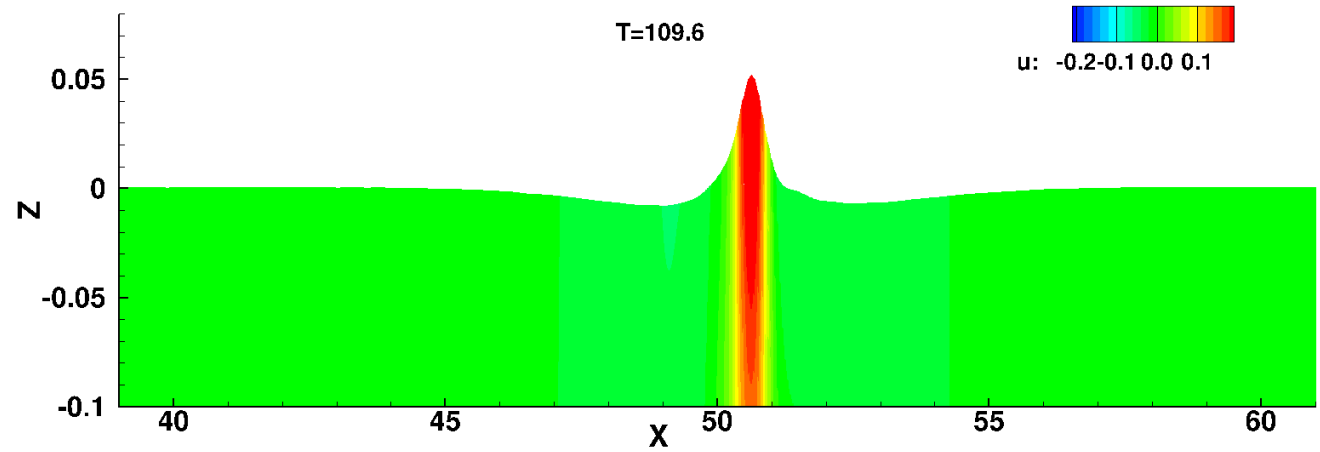
T=109.6
u: -0.2-0.1 0.0 0.1
0.05
0
-0.05
-0.1
Z
40
45
50
55
60
X

(c)

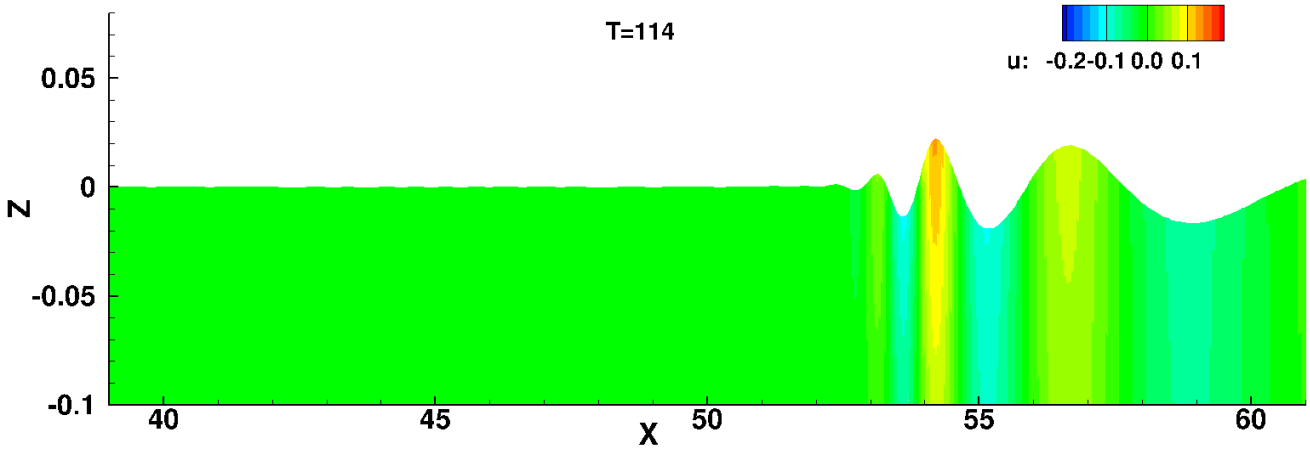

(d)

Figure 10: Snapshots of numerical simulation at different time steps for the flat bottom experimental case (Run 202002). Observe that a fast moving wave group is overtaking a slow moving wave group, resulting in wave focussing at $t = 109.56s$ and $x = 50.75m$. In Fig. 13(a) we show the complete domain, Fig. 13(b) – 13(d) details near the free surface.

formation in the shallow water equations then provides the necessary wave damping. Some preliminary work on coupling the numerical models for deep and shallow water waves has already been done by us in collaboration with F.A. Klaver.

6. Acknowledgements

We acknowledge financial support of the Technology Foundation STW for the project "Complex wave-current interactions in a numerical wave tank" and The Netherlands Organisation for Scientific Research (NWO) for the project "Compatible Mathematical Models for Coastal Hydrodynamics". We are grateful to the Maritime Research Institute Netherlands for providing the data of the laboratory experiments.

Appendix A. Evaluation of finite element matrices

In this section we will discuss some aspects of the construction of the finite element matrices. We will assume that a structured mesh is used. The prescribed horizontal movement of the piston-type wave maker is denoted as $r(t)$. The free surface wave height at the free surface node with index k at time t is $\eta(x_k, t)$. The computational mesh in the flow domain $\Omega_h(t)$, then is obtained by moving each node i according to:

$$x_i(t) = x_i(0) + \gamma_{x,i} r(t) \quad \text{and} \quad z_i(t) = z_i(0) + \gamma_{z,i}\eta(x_k, t), \tag{A.1}$$

with the multiplication factors $\gamma_{x,i} := \big(L - x_i(0)\big)/L$ and $\gamma_{z,i} := \big(H + z_i(0)\big)/H$.

For the evaluation of the matrices in the discrete formulation we first consider now the free surface S_F^n of the domain Ω^n. The free surface elements are denoted as $\bar{K}_m$, with m the element

index. Each free surface finite element $\bar{K}_m$ is mapped to a reference element $\bar{K} = [-1, 1]$ using the transformation $\bar{F}_s : \bar{K} \mapsto \bar{K}_m$, defined as

$$\bar{F}_s : \bar{K} \to \bar{K}_m : \zeta \mapsto x = \hat{x}_{m,\beta}(t)\hat{\psi}_\beta(\zeta), \tag{A.2}$$

where $\beta = 1, 2$ denote the local node numbers of $\bar{K}_m$ and $\hat{x}_{m,\beta}(t)$ the coordinates of the free surface element. The subscript (m, β) refers to the global node number k, and $\zeta \in [-1, 1]$ is the coordinate of the reference element $\bar{K}$. The standard shape functions of the reference element $\bar{K}$ are defined as

$$\hat{\psi}_1 = \frac{1}{2}(1 - \zeta) \quad \text{and} \quad \hat{\psi}_2 = \frac{1}{2}(1 + \zeta). \tag{A.3}$$

We compute the Jacobian of the surface element transformation (A.2) as

$$\bar{J}_{s,m} = \frac{\partial x}{\partial \zeta} = \hat{x}_{m,1}(t)\frac{\partial \hat{\psi}_1}{\partial \zeta} + \hat{x}_{m,2}(t)\frac{\partial \hat{\psi}_2}{\partial \zeta} = \frac{1}{2}(\hat{x}_{m,2}(t) - \hat{x}_{m,1}(t)) = \frac{1}{2}\Delta x_m(t). \tag{A.4}$$

This relation shows that the Jacobian is time-dependent, since the horizontal mesh size changes every time step due to the wave maker movement. The gradients of the surface basis functions are equal to

$$\begin{pmatrix} \dfrac{\partial \varphi_{s,m,\beta}}{\partial t} \\ \dfrac{\partial \varphi_{s,m,\beta}}{\partial x} \end{pmatrix} = \frac{1}{|\bar{J}_{s,m}|} \begin{pmatrix} \dfrac{\partial x}{\partial \zeta} & -\dfrac{\partial x}{\partial t} \\ 0 & 1 \end{pmatrix} \begin{pmatrix} 0 \\ \dfrac{\partial \hat{\psi}_\beta}{\partial \zeta} \end{pmatrix} = \frac{1}{|\bar{J}_{s,m}|} \begin{pmatrix} -\dfrac{\partial(\hat{x}_{m,\alpha}\hat{\psi}_\alpha)}{\partial t}\dfrac{\partial \hat{\psi}_\beta}{\partial \zeta} \\ \dfrac{\partial \hat{\psi}_\beta}{\partial \zeta} \end{pmatrix}. \tag{A.5}$$

The time derivative of the horizontal coordinate of a free surface node can now be computed using its dependence on the wave maker position, given by (A.1),

$$\frac{\partial \hat{x}_{m,\beta}}{\partial t} = \gamma_{x,m,\beta}\frac{\mathrm{d}r}{\mathrm{d}t}. \tag{A.6}$$

This relation shows that the time derivative of the horizontal coordinate is proportional to the wave maker velocity. This allows us to evaluate the time derivative in (A.5) and the matrix D_{kl} in (16).

The global matrices D_{kl} and M_{kl} in (16) are now computed as follows:

$$D_{kl} := \sum_{\forall \bar{K}_m \subset S_F} \int_{\bar{K}} \hat{\psi}_\alpha(\gamma_{x,m,1}\hat{\psi}_1 + \gamma_{x,m,2}\hat{\psi}_2)\frac{\partial \hat{\psi}_\beta}{\partial \zeta}\frac{\mathrm{d}r}{\mathrm{d}t}\mathrm{d}\zeta, \tag{A.7}$$

$$M_{kl} := \sum_{\forall \bar{K}_m \subset S_F} \int_{\bar{K}} \hat{\psi}_\alpha \hat{\psi}_\beta |\bar{J}_{s,m}| \mathrm{d}\zeta, \tag{A.8}$$

with the global node numbers $k = (m, \alpha)$ and $l = (m, \beta)$ of points at the free surface.

We also define finite elements $\bar{K}_m(t)$ on the piston wave maker S_W, given by the vertical domain $\{r(t)\} \times [-H, \eta]$. Each wave maker finite element $\bar{K}_w$ is mapped to the reference element $\bar{K}$ using

the transformation $\bar{F}_w : \bar{K} \mapsto \bar{K}_m$ defined as

$$\bar{F}_w : \bar{K} \to \bar{K}_m : \zeta \mapsto z := \hat{z}_{m,\beta}(t)\hat{\psi}_\beta(\zeta); \tag{A.9}$$

where, $\beta = 1, 2$ denote the local node numbers of element $\bar{K}_m$. The subscript (m, β) connects to global node number k of nodes at the wave maker and $\hat{z}_{m,\beta}(t)$ are the coordinates of the wave maker element. We compute the Jacobian of the transformation (A.9) at the nodes $m \in \mathcal{N}_W$ as

$$J_{w,m} = \frac{\partial z}{\partial \zeta} = \hat{z}_{m,1}\frac{\partial \psi_1}{\partial \zeta} + \hat{z}_{m,2}\frac{\partial \psi_2}{\partial \zeta} = \frac{1}{2}(\hat{z}_{m,2} - \hat{z}_{m,1}) = \frac{1}{2}\Delta z_m. \tag{A.10}$$

The global vector W_k in (16) is now computed as:

$$W_k := \sum_{\forall \bar{K}_m \subset S_W} \int_{\bar{K}} \frac{\mathrm{d}r}{\mathrm{d}t}\hat{\psi}_\beta |J_{w,m}| \mathrm{d}\zeta, \tag{A.11}$$

with the global node number $k = (m, \beta)$.

Appendix B. Variations of the kinetic energy

Given the prescribed wave maker motion the variations of the x-coordinates of the nodes are defined as

$$\delta x_i = \delta\big(x_i(0) + \gamma_{x,i} r(t)\big) = \gamma_{x,i}\delta(r(t)) = 0. \tag{B.1}$$

The variations of the z coordinates are connected with the free surface node as

$$\delta z_i = \delta\big(z_i(0) + \gamma_{z,i}\eta_k\big) = \gamma_{z,i}\delta\eta_k. \tag{B.2}$$

Using the definition given in (16), we can compute the variations of the matrix A_{ij} then as

$$\begin{aligned}
\delta A_{ij}(\boldsymbol{\eta}) &= \delta \sum_{K_m^n \in \bar{\mathcal{T}}_h^n} \int_{K_m^n} (\nabla\varphi_i \cdot \nabla\varphi_j)\mathrm{d}x\mathrm{d}z \\
&= \sum_{K_m^n \in \bar{\mathcal{T}}_h^n} \Big(\frac{1}{|J_m|}\Big) \begin{pmatrix} \dfrac{\partial \hat{\psi}_\alpha}{\partial \zeta_1} \\ \dfrac{\partial \hat{\psi}_\alpha}{\partial \zeta_2} \end{pmatrix}^T \begin{bmatrix} 2\Big(\dfrac{\partial z}{\partial \zeta_2}\Big)\delta z_{\zeta_2} & -\dfrac{\partial z}{\partial \zeta_1}\delta z_{\zeta_2} - \dfrac{\partial z}{\partial \zeta_2}\delta z_{\zeta_1} \\ \dfrac{\partial z}{\partial \zeta_1}\delta z_{\zeta_2} + \dfrac{\partial z}{\partial \zeta_2}\delta z_{\zeta_1} & 2\Big(\dfrac{\partial z}{\partial \zeta_1}\Big)\delta z_{\zeta_1} \end{bmatrix} \begin{pmatrix} \dfrac{\partial \hat{\psi}_\beta}{\partial \zeta_1} \\ \dfrac{\partial \hat{\psi}_\beta}{\partial \zeta_2} \end{pmatrix} \mathrm{d}\zeta_1\mathrm{d}\zeta_2 \\
&- \sum_{K_m^n \in \bar{\mathcal{T}}_h^n} \Big(\frac{\delta|J_m|}{|J_m|^2}\Big) \begin{pmatrix} \dfrac{\partial \hat{\psi}_\alpha}{\partial \zeta_1} \\ \dfrac{\partial \hat{\psi}_\alpha}{\partial \zeta_2} \end{pmatrix}^T \begin{bmatrix} \Big(\dfrac{\partial z}{\partial \zeta_2}\Big)^2 - \Big(\dfrac{\partial x}{\partial \zeta_2}\Big)^2 & -\dfrac{\partial z}{\partial \zeta_1}\dfrac{\partial z}{\partial \zeta_2} + \dfrac{\partial x}{\partial \zeta_1}\dfrac{\partial x}{\partial \zeta_2} \\ \dfrac{\partial z}{\partial \zeta_1}\dfrac{\partial z}{\partial \zeta_2} - \dfrac{\partial x}{\partial \zeta_1}\dfrac{\partial x}{\partial \zeta_2} & \Big(\dfrac{\partial z}{\partial \zeta_1}\Big)^2 - \Big(\dfrac{\partial x}{\partial \zeta_1}\Big)^2 \end{bmatrix} \begin{pmatrix} \dfrac{\partial \hat{\psi}_\beta}{\partial \zeta_1} \\ \dfrac{\partial \hat{\psi}_\beta}{\partial \zeta_2} \end{pmatrix} \mathrm{d}\zeta_1\mathrm{d}\zeta_2,
\end{aligned} \tag{B.3}$$

with the global node numbers $i = (m, \alpha)$ and $j = (m, \beta)$ of points in the computational mesh. The Jacobian matrix of the mapping $F_m^n : \hat{K} \to K_m^n$ is

$$J_m = \begin{pmatrix} \dfrac{\partial x}{\partial \zeta_1} & \dfrac{\partial x}{\partial \zeta_2} \\ \dfrac{\partial z}{\partial \zeta_1} & \dfrac{\partial z}{\partial \zeta_2} \end{pmatrix}$$

and the variations δz_{ζ_1} and δz_{ζ_2} are equal to

$$\begin{aligned}
\delta z_{\zeta_1} =& -\frac{1-\zeta_2}{4}\delta z_{m,1} + \frac{1-\zeta_2}{4}\delta z_{m,2} + \frac{1+\zeta_2}{4}\delta z_{m,3} - \frac{1+\zeta_2}{4}\delta z_{m,4} \\
=& \big(-\gamma_{z,m,1}\frac{1-\zeta_2}{4} - \gamma_{z,m,4}\frac{1+\zeta_2}{4}\big)\delta\eta_k + \big(\gamma_{z,m,2}\frac{1-\zeta_2}{4} + \gamma_{z,m,4}\frac{1+\zeta_2}{4}\big)\delta\eta_{k+1}, \\
\delta z_{\zeta_2} =& -\frac{1-\zeta_1}{4}\delta z_{m,1} - \frac{1+\zeta_1}{4}\delta z_{m,2} + \frac{1+\zeta_1}{4}\delta z_{m,3} + \frac{1-\zeta_1}{4}\delta z_{m,4} \\
=& \big(-\gamma_{z,m,1}\frac{1-\zeta_1}{4} + \gamma_{z,m,4}\frac{1-\zeta_1}{4}\big)\delta\eta_k + \big(-\gamma_{z,m,2}\frac{1+\zeta_1}{4} + \gamma_{z,m,3}\frac{1+\zeta_1}{4}\big)\delta\eta_{k+1}.
\end{aligned} \tag{B.4}$$

Here, we assume that the first and fourth vertices of the element K_m^n are on the vertical grid line connected to the free surface node k. Similarly, the second and third element vertex are connected to the free surface node $k+1$. The crucial part of these relations is that variations in the free surface are coupled to variations in the mesh. This dependency should not be ignored in computing the variations of the Miles functional. Otherwise, incorrect dynamical equations are obtained, which will become unstable for large amplitude wave motion.

Finally, the variations of the Jacobian are given by

$$\delta|J_m| = (\partial x/\partial\zeta_1)\delta z_{\zeta_2} - (\partial x/\partial\zeta_2)\delta z_{\zeta_1}. \tag{B.5}$$

After the substitution of (B.5) into (B.3) we obtain the explicit expression for C_{kij} in (27).

Similarly, variations of the wave maker contribution with respect to the wave height η are equal to

$$\delta W_e(\boldsymbol{\eta}_s) = \delta \int_{\bar{\Gamma}_W^n} \frac{\mathrm{d}r}{\mathrm{d}t}\varphi_e \mathrm{d}z = \sum_{\forall \bar{K}_m \subset S_W} \int_{\bar{K}} \frac{\mathrm{d}r}{\mathrm{d}t}\psi_\alpha \delta|J_{w,m}|\mathrm{d}\zeta_2, \tag{B.6}$$

where e is the global node number of (m, α), and the variations of the Jacobian $|J_{w,m}|$ are given by

$$\delta|J_{w,m}| = \delta\big(\frac{1}{2}(z_{m,2} - z_{m,1})\big) = \frac{1}{2}(\gamma_{z,m,2} - \gamma_{z,m,1})\delta\eta_s, \tag{B.7}$$

with $s \in \mathcal{N}_F \cap \mathcal{N}_W$. Finally, substituting (B.7) into (B.6) gives (29).

References

[1] D.N. Arnold, F. Brezzi, B. Cockburn and L.D. Marini, Unified analysis of discontinuous Galerkin methods for elliptic problems, SIAM J. Numer. Anal. 39(5) (2002) 1749–1779.

[2] J.T. Beale, A convergent boundary integral method for three-dimensional water waves, Math. Comp. 70 (2001) 977–1029.

[3] J. Broeze, E.F.G. van Daalen and P. J. Zandbergen, A three-dimensional panel method for nonlinear free surface waves on vector computers, Comput. Mech. 13 (1993) 12–28.

[4] G. Dal Maso, P.G. Le Floch and F. Murat, Definition and weak stability of nonconservative products, J. de Mathématiques Pures et Appliquées 74(6) (1995) 483–548.

[5] C. Fochesato and F. Dias, A fast method for nonlinear three-dimensional free-surface waves, Proc. R. Soc. A. 462 (2006) 2715–2735.

[6] C.F. Fochesato, S. Grilli, F. Dias, Numerical modeling of extreme rogue waves generated by directional energy focusing, Wave Motion 44 (2007) 395–416.

[7] J.D. Fenton and M.M. Rienecker, A Fourier method for solving nonlinear water-wave problems: application to solitary-wave interactions, J. Fluid Mech. 118 (1982) 411–443.

[8] E. Gagarina, J.J.W. van der Vegt, V.R. Ambati, and O. Bokhove, A Hamiltonian Boussinesq model with horizontally sheared currents, in: Proc. 3rd Int. Symp. on Shallow Flows, June 4-6, 2012, Iowa, USA. http://purl.utwente.nl/publications/79724

[9] E. Gagarina, J.J.W. van der Vegt, and O. Bokhove, Horizontal circulation and jumps in Hamiltonian wave models, Accepted: *Nonlin. Processes Geophys.*, 2013. http://eprints.eemcs.utwente.nl/22919

[10] E. van Groesen, T. Bunnik, A. Andonowati, Surface wave modelling and simulation for wave tanks and coastal areas, in: Proc. Int. Conf. on Developments in Marine CFD, November 18 19, 2011, Chennai, India.

[11] E. Guerber, M. Benoit, S.T. Grilli, C. Buvat, A fully nonlinear implicit model for wave interactions with submerged structures in forced or free motion, Eng. Anal. with Bound. Elem. 36 (2012) 1151–1163.

[12] J. Hennig and C.E. Schmittner, Experimental variation of focussing wave groups for the investigation of their predictability, in: Proc. 28th Int. Conf. OMAE, May 31-June 5, 2009, Hawaii, USA.

[13] E. Hairer, C. Lubich and G. Wanner, Geometric numerical integration, Second Ed., Springer, Berlin, 2006.

[14] T. Hou and P. Zhang, Convergence of a boundary integral method for 3-D water waves, SIAM J. Numer. Anal. 2 (2002) 1–34.

[15] R.S. Johnson, A modern introduction to the mathematical theory of water waves, Cambridge University Press, Cambridge, 1997.

[16] J.W. Kim and K.J. Bai, A finite element method for two dimensional water wave problems. Int. J. Numer. Methods Fluids 30(1) (1999) 105–121.

[17] J.W. Kim, K.J. Bai, R.C. Ertekin, and W.C. Webster, A strongly-nonlinear model for water waves in water of variable depth – The irrotational Green-Naghdi model, J. Offshore Mech. Arct. Eng. 125(1) (2003) 25–32.

[18] G. Klopman, M. Dingemans and E. van Groesen, A variational model for fully non-linear water waves of Boussinesq type, in: Proc. 20th International Workshop on Water Waves and Floating Bodies, May 29-June 1, 2005, Spitsbergen, Norway.

[19] A.L. Latifah and E. van Groesen, Coherence and predictability of extreme events in irregular waves, Nonlin. Processes Geophys. 19 (2012) 199–213.

[20] M. Lesoinne and C. Farhat, Geometric conservation laws for flow problems with moving boundaries and deformable meshes, and their impact on aeroelastic computations, Comput. Meth. Appl. Mech. Engng 134 (1996) 71–90.

[21] M.S. Longuet-Higgins and E.D. Cokelet, The deformation of steep surface waves on water, I. A numerical method of computation, Proc. Roy. Soc. London A 35 (1976) 1–26.

[22] J.C. Luke, A variational principle for a fluid with a free surface, J. Fluid Mech. 27(2) (1967) 395–397.

[23] Q.W. Ma, G.X. Wu and R. Eatock Taylor, Finite element simulation of fully nonlinear interaction between vertical cylinders and steep waves. Part 2: Methodology and numerical procedure, Int. J. Numer. Meth. Fluids, 36 (2001) 265–285.

[24] Q.W. Ma, G.X. Wu and R. Eatock Taylor, Finite element simulation of fully nonlinear interaction between vertical cylinders and steep waves. Part 1: Numerical results and validation, Int. J. Numer. Meth. Fluids 36 (2001) 287–308.

[25] Q.W. Ma and S. Yan, Quasi ALE finite element method for nonlinear water waves, J. Comput. Phys. 212 (2006) 52–72.

[26] J.W. Miles, On Hamilton's principle for surface waves, J. Fluid Mech. 83(1) (1977) 153–158.

[27] S. Rhebergen, O. Bokhove and J.J.W. van der Vegt, Discontinuous Galerkin finite element methods for hyperbolic nonconservative partial differential equations. J. Comp. Phys. 227(3) (2008) 1887–1922.

[28] S. Rhebergen, Discontinuous Galerkin finite element methods for (non)conservative partial differential equations. Ph.D. Thesis, University of Twente, Enschede, The Netherlands, 2010.

[29] J.E. Romate and P.J. Zandbergen, Boundary integral equation formulations for free-surface flow problems in two and three dimensions, Comput. Mech. 4(4) (1989) 267–282.

[30] B. Satish, B. Kris, E. Victor, D.G. William, K. Dinesh, G.K. Matthew, McInnes C. Lois, B.F. Smith and Z. Hong, PETSc users manual, Argonne National Laboratory, NL-95/11 - Revision 2.1.5, 2004. http://www-unix.mcs.anl.gov/petsc

[31] B. Satish, B. Kris, D.G. William, K. Dinesh, G.K. Matthew, McInnes C. Lois, B.F. Smith and Z. Hong, PETSc Web page, 2001. http://www.mcs.anl.gov/petsc

[32] B. Satish, D.G. William, McInnes C. Lois and B.F. Smith, Efficient management of parallelism in object oriented numerical software libraries, In modern software tools in scientific computing by E. Arge, A.M. Bruaset and H.P. Langtangen, Birkhäuser Press, 163–202, 1997.

[33] S.K. Tomar and J.J.W. van der Vegt, Runge-Kutta discontinuous Galerkin method for linear free-surface gravity waves using high order velocity recovery, Comput. Meth. Appl. Mech. and Engng. 196(13-16) (2007) 1984–1996.

[34] W. Tsai and D. Yue, Computations of nonlinear free-surface flows, Ann. Rev. Fluid Mech. 28 (1996) 249–278.

[35] J.J.W. van der Vegt and S.K. Tomar, Discontinuous Galerkin method for linear free surface gravity waves, J. Sci. Comput. 22(1) (2005) 531–567.

[36] J.J.W. van der Vegt and H. van der Ven, Space-time discontinuous Galerkin finite element method with dynamic grid motion for inviscid compressible flows, J. Comput. Phys. 182 (2002) 546–585.

[37] J.J.W. van der Vegt and Y. Xu, Space-time discontinuous Galerkin method for nonlinear water waves, J. Comput. Phys. 224(1) (2007) 17–39.

[38] T. Vinje and P. Brevig, Numerical simulation of breaking waves, Adv. Water Resources 4 (1981) 77–82.

[39] J.H. Westhuis, The numerical simulation of nonlinear water waves in a hydrodynamic model test basin, Ph.D. thesis, University of Twente, Enschede, The Netherlands, 2001.

[40] G.X. Wu and Z.Z. Hu, Simulation of nonlinear interactions between waves and floating bodies through a finite-element based numerical tank, Proc. R. Soc. Lond. Se. A 460 (2004) 2797–2817.

[41] G.Z. Wang and C.X. Wu, Interactions between fully nonlinear water waves and cylinder arrays in a wave tank, Ocean. Engng. 37 (2010) 400–417.

[42] G.Z. Wang and C.X. Wu, A brief summary of finite element method applications to nonlinear wave-structure interactions, J. Marine Sci. Appl. 10 (2011) 127–138.